

Classical and quantum spin dynamics of the honeycomb Γ modelAnjana M. Samarakoon,^{1,2} Gideon Wachtel,^{3,4} Youhei Yamaji,^{5,6} D. A. Tennant,^{7,2}
Cristian D. Batista,^{1,2,8} and Yong Baek Kim^{3,9,10}¹*Neutron Scattering Division, Oak Ridge National Laboratory, Oak Ridge, Tennessee 37831, USA*²*Shull-Wollan Center, Oak Ridge National Laboratory, Oak Ridge, Tennessee 37831, USA*³*Department of Physics, University of Toronto, Toronto, Ontario, Canada, M5S 1A7*⁴*Racah Institute of Physics, The Hebrew University, Jerusalem 91904, Israel*⁵*Department of Applied Physics, The University of Tokyo, Hongo, Bunkyo-ku, Tokyo 113-8656, Japan*⁶*JST PRESTO, Hongo, Bunkyo-ku, Tokyo 113-8656, Japan*⁷*Materials Science and Technology Division, Oak Ridge National Laboratory, Oak Ridge, Tennessee 37831, USA*⁸*Department of Physics and Astronomy, University of Tennessee, Knoxville, Tennessee 37996-1200, USA*⁹*Canadian Institute for Advanced Research, Quantum Materials Program, Toronto, Ontario, Canada, M5G 1M1*¹⁰*School of Physics, Korea Institute for Advanced Study, Seoul 130-722, Korea*

(Received 26 March 2018; published 16 July 2018)

Quantum-to-classical crossover is a fundamental question in dynamics of quantum many-body systems. In frustrated magnets, for example, it is highly nontrivial to describe the crossover from the classical spin liquid with a macroscopically degenerate ground-state manifold to the quantum spin liquid phase with fractionalized excitations. This is an important issue, as we often encounter the demand for a sharp distinction between the classical and quantum spin liquid behaviors in real materials. Here we take the example of the classical spin liquid in a frustrated magnet with novel bond-dependent interactions to investigate the classical dynamics, and critically compare it with quantum dynamics in the same system. In particular, we focus on signatures in the dynamical spin structure factor. Combining Landau-Lifshitz dynamics simulations and the analytical Martin-Siggia-Rose approach, we show that the low-energy spectra are described by relaxational dynamics and highly constrained by the zero mode structure of the underlying degenerate classical manifold. Further, the higher energy spectra can be explained by precessional dynamics. Surprisingly, many of these features can also be seen in the dynamical structure factor in the quantum model studied by finite-temperature exact diagonalization. We discuss the implications of these results and their connection to recent experiments on frustrated magnets with strong spin-orbit coupling.

DOI: [10.1103/PhysRevB.98.045121](https://doi.org/10.1103/PhysRevB.98.045121)**I. INTRODUCTION**

The crossover between classical and quantum regimes in frustrated magnets has been an important theoretical question in the last few decades. This issue is particularly important in understanding the nature of the quantum spin liquid phases which may arise at low temperature due to extreme quantum fluctuations. In the classical regime, there may exist a window of temperatures below the Curie-Weiss scale where the correlated spin moments are thermally fluctuating within the degenerate manifold of classical ground states. This is the cooperative paramagnetic state, or the so-called classical spin liquid. In the quantum regime, it is clearly not possible to maintain such a state down to zero temperature as the quantum ground state should be unique (up to a topological degeneracy in the case of quantum spin liquids). An important question is how much information about the degenerate manifold of classical ground states is encoded in the emergent quantum spin liquid at zero and low temperatures. Such a question may be especially relevant for two-dimensional spin liquid phases which show no finite-temperature phase transition, but only crossovers.

One natural place to look for the clue for this question is the dynamical spin correlation or the dynamical spin structure factor. A recent work on the Kitaev model [1] in two

dimensions investigates the dynamical spin correlations of the classical Kitaev model via Landau-Lifshitz (LL) dynamics [2]. The resulting dynamical structure factor was compared with that of the quantum model [3–5], which is exactly solvable and supports a quantum spin liquid ground state with gapless Majorana fermion excitations. There exist two crossover temperatures, T_v and T_Q , in the Kitaev model on the honeycomb lattice, as seen in the specific heat [6]. At $T < T_v$, the vision or flux gap is larger than the temperature scale so that the system is essentially characterized by the zero-temperature ground state. When $T_v < T < T_Q$, the flux degree of freedom is thermally disordered, but the Majorana fermions are still well defined. For $T > T_Q$, the system crosses over to the classical regime. It was found that the dynamical spin correlations in the quantum model at $T > T_v$ are remarkably similar to those of the cooperative paramagnetic regime of the classical model at finite temperature. Moreover, the dynamical structure factor of the quantum model knows about the zero mode structure of the classically degenerate manifold, even when $T_v < T < T_Q$. This suggests that all the classically degenerate spin states are participating in the quantum fluctuations down to $T \approx T_v$, which eventually leads to the emergence of the quantum spin liquid phase at low temperature $T < T_v$.

In principle, it is not necessary that the full degenerate manifold of the classical states is involved in the formation of the quantum spin liquid at low temperature, since thermal entropy or zero-point quantum fluctuations may select a subset of the full degenerate manifold at some intermediate temperature. On the other hand, when the full degenerate manifold is participating in quantum fluctuations at low temperature, as in the case of the Kitaev model for $T_v < T < T_Q$, and if the spin correlations remain short-ranged, it is highly suggestive that the zero-temperature ground state would indeed be a quantum spin liquid. An alternative choice for the zero-temperature ground state could be a magnetically ordered state or a quantum critical point, which would show the development of long-range dynamical spin fluctuations. In the case of the Kitaev model, we already know that this is not the case and that the zero-temperature ground state is a quantum spin liquid. One may, however, be able to use this lesson to infer the possible presence of a quantum spin liquid in models which are not exactly solvable.

In the current work, we investigate the dynamical spin correlations in the classical and quantum Γ model [7] (defined below) on the honeycomb lattice, which is known to possess a macroscopically degenerate manifold of classical ground states [8], while the quantum model is not exactly solvable. This model represents the bond-dependent anisotropic and symmetric spin interactions on the honeycomb lattice:

$$\mathcal{H} = \Gamma \sum_{\alpha \neq \beta \neq \gamma} \sum_{(\mathbf{r}, \mathbf{r}') \in \gamma} (S_r^\beta S_{r'}^\alpha + S_r^\alpha S_{r'}^\beta), \quad (1)$$

where S_r^α are spin operators at sites \mathbf{r} of a honeycomb lattice, and $\alpha, \beta, \gamma = x, y, z$. Such interactions (as well as the Kitaev interaction mentioned above) arise in strongly spin-orbit-coupled Mott insulators such as Li_2IrO_3 and $\alpha\text{-RuCl}_3$, where Ir^{4+} or Ru^{3+} ions form effective $J = 1/2$ local moments. Currently, the relative importance of the Kitaev and Γ interactions is an important issue in theoretical and experimental investigations of this class of Kitaev-like materials [7,9–23]. For instance, the dominance of one of these interactions or the cooperation of these two interactions may lead to the possible emergence of quantum spin liquid in these materials, especially in the presence of external pressure or magnetic field.

We first use the Landau-Lifshitz dynamics to compute the dynamical structure factor in the classical model at finite temperature. It is shown that the zero mode structure of the degenerate manifold of classical ground states is reflected in the low-frequency part of the dynamical spin fluctuation spectra. For example, in the case of the antiferro-sign of the $\Gamma > 0$ interaction, the structure factor at low frequencies is suppressed at the Γ and X points of the Brillouin zone, which we explain using the constraints on the classical spin states which belong to the degenerate manifold. Next, we employ the Martin-Siggia-Rose (MSR) formulation of Langevin dynamics to further understand the nature of the dynamical spin correlations. These two different methods lead to essentially the same dynamical spin correlations, leading to the conclusion that the system itself may be acting as an effective thermal bath. Furthermore, it is shown that the low-frequency response is relaxational and reflects the zero mode structure, while the higher-frequency response is mostly precessional, and some characteristic

precessional modes exist at finite frequencies. The evolution of dynamical spin correlations is also investigated as a function of temperature for the comparison with the quantum model.

The dynamical spin structure factor in the quantum Γ model is studied by exact diagonalization via the shifted Krylov subspace method, which is combined with a typical quantum state approach at finite temperature. In previous studies [24], it was shown that there exist two crossover temperatures, $T_1 \approx 0.03\Gamma$ and $T_2 \approx 0.4\Gamma$, in the specific heat, similar to the case of the Kitaev model. T_2 marks the crossover from the high-temperature classical regime to the quantum regime. We find that the dynamical spin correlations at low frequencies in the quantum model show distinct signatures of the zero mode structure of the degenerate manifold of classical ground states even when $T_1 < T < T_2$, which gradually crosses over to the low-temperature extreme quantum limit for $T < T_1$. This behavior is reminiscent of the dynamical spin correlations in the Kitaev model, where correlations as a function of temperature are remarkably similar to the classical result. This means that the short-range spin fluctuations from the degenerate manifold persist even in the quantum regime of $T_1 < T < T_2$. On the other hand, the dynamical spin correlations at zero temperature, while they remain short ranged, show features that are not present in the classical model. In the case of the Γ model, we currently do not know what the quantum ground state is. One possibility is that below a certain temperature a symmetry is broken due to order by quantum disorder [8]. Interestingly, however, recent density-matrix renormalization group and exact diagonalization studies suggest the possible presence of a quantum spin liquid ground state in the Γ model [25]. Since we do not have an analytical understanding of the underlying quasiparticles in the Γ model, we cannot make a more precise connection to underlying quantum degrees of freedom, which was possible in the case of the Kitaev model. Nonetheless, the phenomenological similarity to the classical-quantum correspondence in the Kitaev model is striking. We may speculate that the entire degenerate manifold of classical states would participate in quantum fluctuations that lead to the formation of the quantum ground state at zero temperature, such as a quantum spin liquid phase. Our findings will help understanding this outstanding issue and a possible connection to experiments on Kitaev-like materials.

The rest of the paper is organized as follows. In Sec. II, we present numerical results obtained from the LL dynamics of the classical model. Section III describes how qualitatively similar results can be obtained analytically within an MSR formalism. The dynamic correlations of the corresponding quantum model are given in Sec. IV. We conclude with a discussion of our main findings in light of recent experiments in Sec. V, while details of our calculations are relegated to the Appendixes.

II. LANDAU-LIFSHITZ DYNAMICS

We study the dynamical spin correlations of the Γ model, Eq. (1), whereby the spin operators are replaced by classical vectors in the Heisenberg equation of motion. The resulting LL equation of motion is

$$\frac{d\mathbf{S}_r}{dt} = \mathbf{S}_r \times \mathbf{B}_r, \quad (2)$$

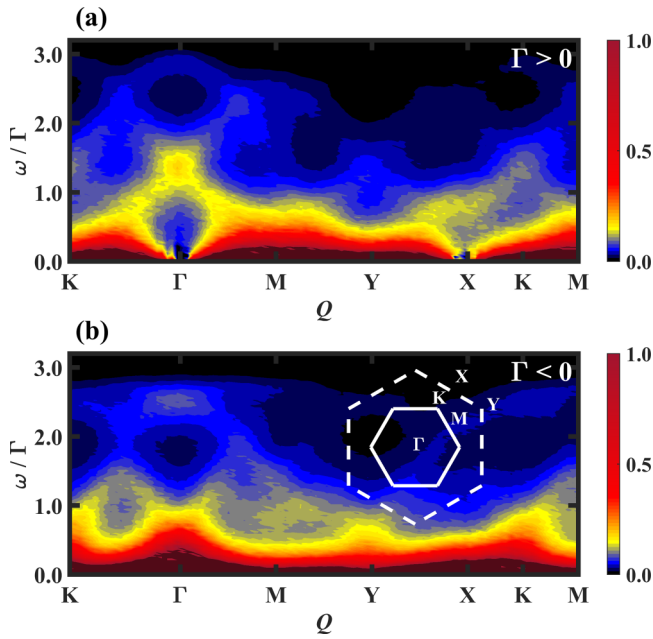


FIG. 1. Trace of the dynamical magnetic structure factor $S(\mathbf{Q}, \omega) = \sum_{\alpha} S^{\alpha\alpha}(\mathbf{Q}, \omega)$ for (a) AFM ($\Gamma > 0$), (b) FM ($\Gamma < 0$) Γ models along the Brillouin zone path, $\mathbf{K} - \Gamma - \mathbf{M} - \mathbf{Y} - \mathbf{X} - \mathbf{K} - \mathbf{M}$, as depicted in the inset.

where \mathbf{B}_r is the molecular field acting on the spin \mathbf{S}_r . This LL equation can be solved numerically by applying a fourth-order Runge-Kutta algorithm with adaptive step size. The average over configurations at a given temperature T is obtained from the Metropolis Monte Carlo sampling method. We note that a closed LL dynamics is more appropriate than Langevin dynamics when the experiment is much faster than the spin-lattice relaxation, which is the typical case in inelastic neutron-scattering experiments. The simulations are performed on a finite lattice of 30×30 unit cells (1800 spins) with periodic boundary conditions.

Figure 1 shows the trace of the dynamical spin structure factor, $S(\mathbf{Q}, \omega) = \sum_{\alpha} S^{\alpha\alpha}(\mathbf{Q}, \omega)$, obtained for the antiferromagnetic (AFM) ($\Gamma > 0$) and ferromagnetic (FM) ($\Gamma < 0$) versions of the Γ model. As expected for a liquid state, $S(\mathbf{Q}, \omega)$ exhibits a continuum of low- and high-frequency modes. The low-frequency (zero) modes arise from the very slow dynamics through different classical ground states. The number of zero modes is macroscopic because of the extensive residual entropy of the ground-state manifold. This dynamics is expected to be *relaxational* because the average of the local field over a period $2\pi/\omega$ is equal to zero. In contrast, the high-frequency modes correspond to the much faster spin precession around the local fields produced by a *given ground-state configuration*. Accordingly, the average of the local fields \mathbf{B}_r over a period $2\pi/\omega$ remains finite.

Both the low- and high-frequency modes contain relevant information about the liquid state. The momentum distribution of the zero-energy modes is a direct consequence of the set of constraints defining the ground-state manifold. Specifically, we show in Appendix A that the Fourier transform $S^{\alpha}(\mathbf{q}) = \sum_r S_r^{\alpha} e^{i\mathbf{q}\cdot\mathbf{r}}$ of any state S_r^{α} in the ground-state manifold vanishes for both $\mathbf{q} = \Gamma$ and $\mathbf{q} = \mathbf{X}$. As a result, the low-energy

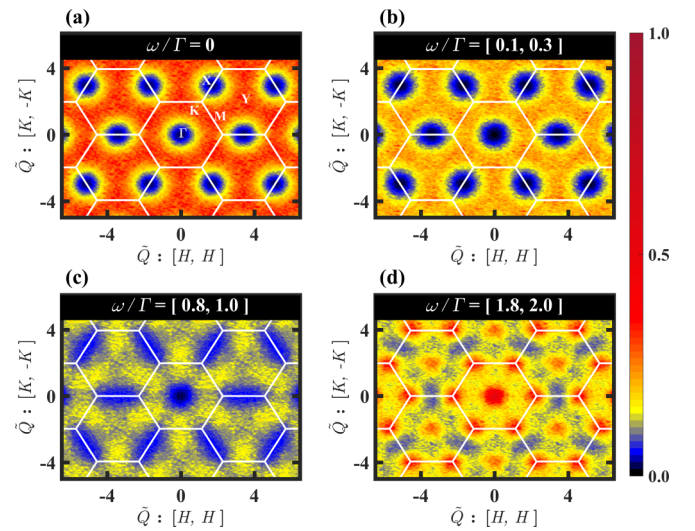


FIG. 2. (a) Elastic component of the trace of the magnetic structure factor $S(\mathbf{Q}, \omega = 0)$. (b)–(d) $S(\mathbf{Q}, \omega)$, integrated over finite energy cuts: (b) $\omega/\Gamma = [0.1, 0.3]$, (c) $\omega/\Gamma = [0.8, 1.0]$, and (d) $\omega/\Gamma = [1.8, 2.0]$.

spectral weight of $S^{\alpha\alpha}(\mathbf{Q}, \omega)$ is suppressed at the Γ and \mathbf{X} points of the Brillouin zone [see Fig. 2(a)]. Correspondingly, as shown in Figs. 2(b)–2(d), the missing low-energy spectral weight at these two points is shifted to frequencies of order Γ . In other words, magnetic excitations with wave vectors Γ and \mathbf{X} are purely precessional. Indeed, as shown in Fig. 2, the precessional modes have the highest intensity at these two wave vectors. As we will see later, the low-energy modes of the quantum $S = 1/2$ model inherit this structure. The high-energy modes contain information about the magnitude and spatial distribution of the instantaneous local fields \mathbf{B}_r of a typical ground-state spin configuration. The dispersion of these modes contains information about the magnetic correlation length of the spin liquid state.

To gain more insight on the structure of the zero-energy modes, we also present the real-space spin-spin correlation function, $S(\mathbf{r}, \omega)$, as a function of ω and T . Figure 3 shows the elastic contribution $S(\mathbf{r}, \omega = 0)$ for different distances up to fifth nearest neighbors (NN) and $T = 10^{-5}\Gamma$. (Calculations need to be done at finite T to have fluctuations and be able to exploit the fluctuation-dissipation theorem.) Remarkably, this is significant only for the on-site and for the

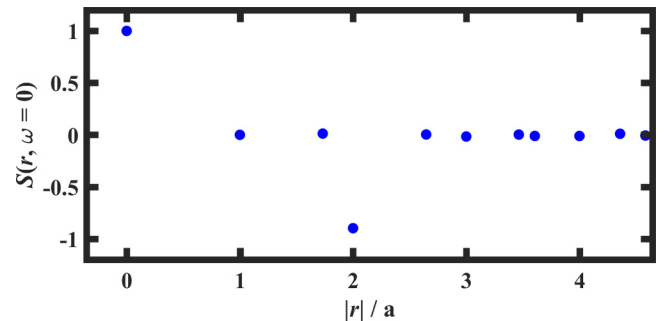


FIG. 3. $S(\mathbf{r}, \omega = 0)$ as a function of $|\mathbf{r}|/a$ (where a is the lattice parameter) at $T = 10^{-5}\Gamma$.

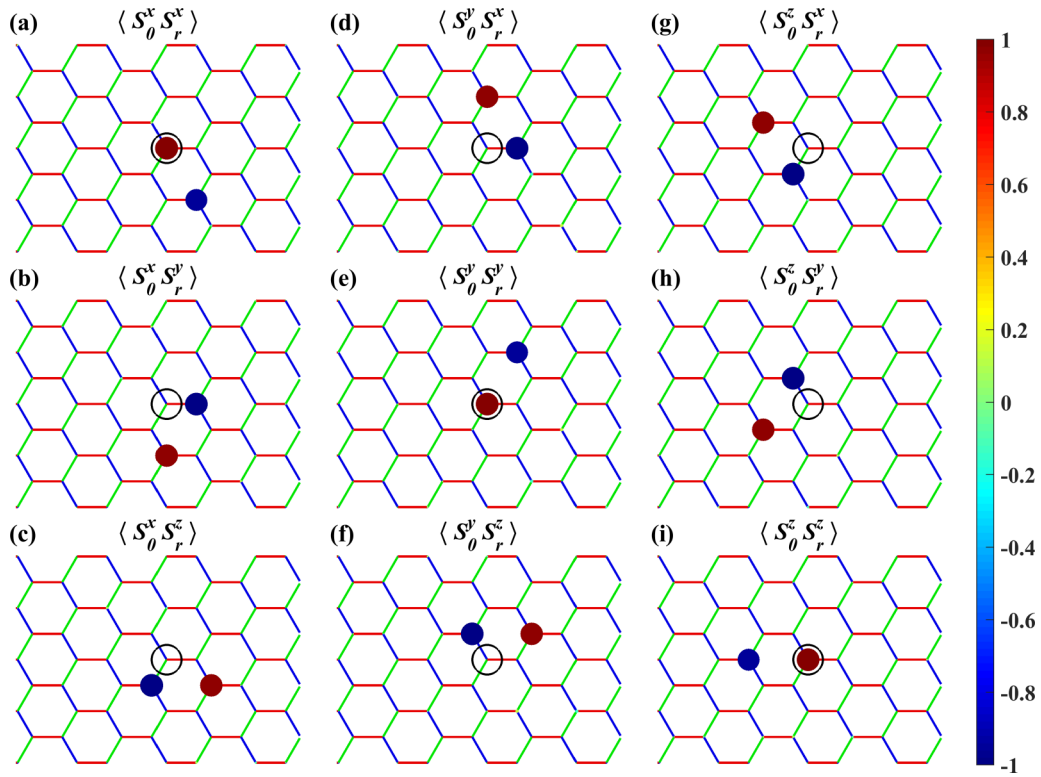


FIG. 4. Static spin-spin correlation function, $\tilde{S}^{\alpha\beta} = \langle S_\theta^\alpha S_r^\beta \rangle = \int S^{\alpha\beta}(\mathbf{r}, \omega) d\omega$, mapped on the real-space lattice with respect to an arbitrary origin denoted by the cross (\times). The temperature of the simulation is $T = 10^{-5}\Gamma$.

third-nearest-neighbor ($|\mathbf{r}|/a = 2$, where a is the lattice parameter) correlation functions. The values obtained for other distances are smaller than the statistical error of the MC calculation. Therefore, the fast exponential decay of the elastic contribution indicates that the magnetic correlation length is of order $2a$.

A similar behavior is observed in the static real-space spin-spin correlation function, $\tilde{S}^{\alpha\beta}(\mathbf{r}) = \langle S_\theta^\alpha S_r^\beta \rangle = \int S^{\alpha\beta}(\mathbf{r}, \omega) d\omega$, shown in Fig. 4. This figure also includes off-diagonal components of the spin-spin correlation function. In all the cases, the correlation function is significant only for distances $|\mathbf{r}|$ equal to or smaller than the separation between third nearest neighbors (opposite sites of each hexagon). Moreover, a subset of the nine spin-spin correlator components $\alpha\beta$ vanishes for any given \mathbf{r} . The form of the real-space correlations, as depicted in Fig. 4, is well accounted for by considering the symmetries of the Hamiltonian, Eq. (1). To show this, we begin by considering the three ways in which one can decompose the honeycomb lattice into hexagon plaquettes, shown in Fig. 5. With each plaquette of a given decomposition we associate six spin components, one from each site around the plaquette. Specifically, a spin component is associated with a neighboring hexagon plaquette if it is of the same type as the bond connecting it with a neighboring plaquette of the same decomposition. There exist three symmetry operations [8], one for each plaquette decomposition, which correspond to π spin rotations about an axis that depends on the sublattice which each spin belongs to. For example, the symmetry operation corresponding to the white plaquettes in Fig. 5 corresponds to a π rotation about the x axis for sublattices 1 and 4,

about the y axis for sublattices 2 and 5, and about the z axis for sublattices 3 and 6. This transformation leaves the spin components $\{S_1^x, S_2^y, S_3^z, S_4^x, S_5^y, S_6^z\}$ invariant (the subscript is the six-sublattice index), while it changes the sign of the other ones. In Appendix B, we show that these symmetries, which are also symmetries of the quantum model, result in vanishing correlations between spin components which are associated with plaquette of different decompositions, according to the rule we just described.

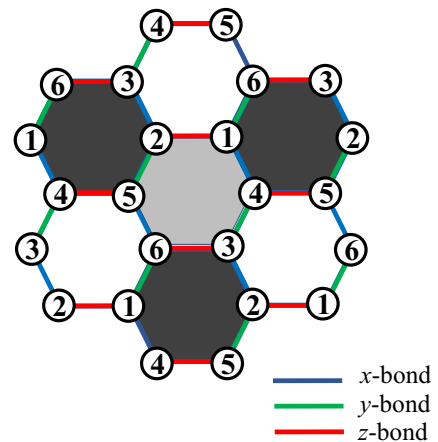


FIG. 5. Six-sublattice decomposition of the honeycomb lattice. We also show the three different decompositions of the lattice into isolated hexagonal plaquettes.

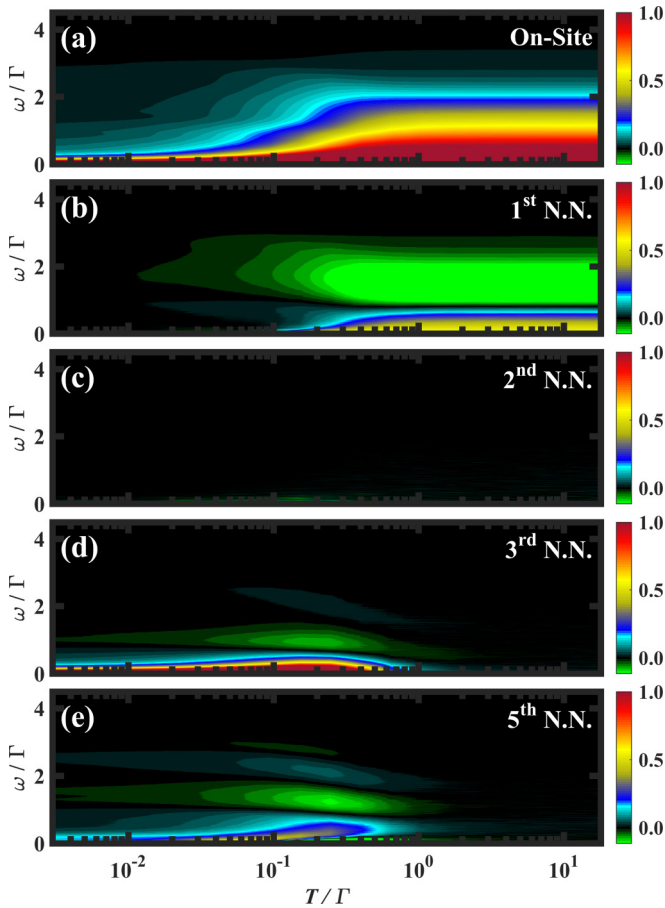


FIG. 6. $S(\mathbf{r}, \omega)$ as a function of temperature and energy ($\hbar\omega$) for AFM ($\Gamma > 0$) Γ model. Panels (a), (d), and (e) show $-S(\mathbf{r}, \omega)$ for \mathbf{r} connecting first, third, and fifth nearest-neighbor sites, respectively. Panel (b) shows $S(\mathbf{r}, \omega)$ for \mathbf{r} connecting nearest-neighbor sites. Panel (c) shows that $S(\mathbf{r}, \omega) = 0$ for \mathbf{r} connecting second-nearest-neighbor sites.

However, the spin-spin correlations are further restricted in the classical limit. Classically, the three components of each spin commute with each other, and as a result, one can define a local transformation that flips the sign of an individual spin component. The classical version of the Γ model is invariant under a *local* symmetry transformation that changes the sign of one spin component of each of the six spins in a *single* hexagon plaquette. The spin component that changes sign is the one corresponding to the only bond which does not connect two spins in the same hexagon [8]. For instance, the symmetry transformation changes the sign of $\{S_1^x, S_2^y, S_3^z, S_4^x, S_5^y, S_6^z\}$ for a *single* white hexagon plaquette. This is the local symmetry that gives rise to the macroscopic degeneracy of the classical ground-state manifold. Consequently, the correlation function $\langle S_0^\alpha S_r^\beta \rangle$ vanishes unless both S_0^α and S_r^β belong to the same single hexagon. This restricts correlations to third neighbor at most and determines the specific components which have nonzero correlations, as seen in Fig. 4. For example, only the diagonal components of the on-site correlations are nonzero, since different components of a given spin are associated with different plaquettes, and thus, uncorrelated. Similarly, the only other nonvanishing diagonal components of the spin-spin

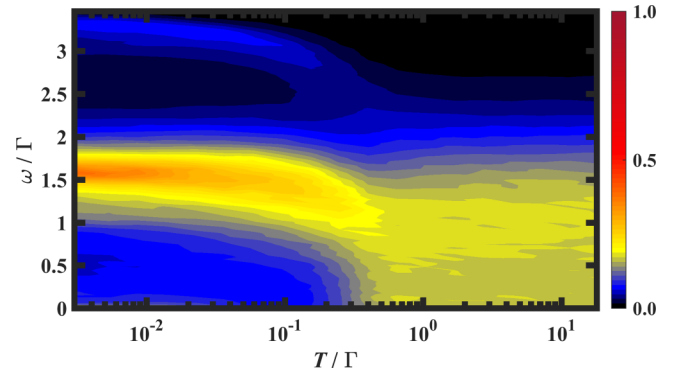


FIG. 7. Temperature evolution of $S(\mathbf{Q} = \Gamma, \omega)$ for AFM ($\Gamma > 0$) Γ model.

correlation function appears for third neighbors, e.g., for the white plaquette mentioned earlier we have only a finite $\langle S_1^y S_4^x \rangle$ in addition to the on-site correlation. Similar considerations restrict finite off-diagonal correlations to nearest and second-nearest neighbors around one plaquette.

Figure 6 shows the temperature and frequency dependence of $S(\mathbf{r}, \omega)$ for several values of \mathbf{r} . In agreement with the symmetry analysis given in Appendix B, $S(\mathbf{r}, \omega)$ vanishes for any frequency when \mathbf{r} connects second-nearest-neighbor sites [see Fig. 6(b)]. The temperature dependence of $S(\mathbf{r}, \omega)$ for other values of \mathbf{r} indicates a crossover from partially precessional to fully diffusive behavior at a temperature of order Γ . The temperature dependence of $S(\mathbf{Q} = \Gamma, \omega)$ shown in Fig. 7 confirms this crossover, indicating that the system evolves continuously from a low-temperature ($T < \Gamma$) correlated liquid (classical Γ liquid) to a high-temperature paramagnetic state.

III. LANGEVIN DYNAMICS

Although, as noted in the previous section, neutron-scattering experiments are faster than spin-lattice relaxation, a Langevin approach may still be used to analytically understand dynamic correlations in LL dynamics. The nonlinear nature of Eq. (2) gives rise to strong relaxation due to inelastic processes, in addition to the more direct precessional dynamics. In other words, the fluctuating spins act as their own heat bath, leading to strong relaxation. At a phenomenological level, it is possible to capture the two types of spin dynamics in a generalized Langevin equation, where a linear term describes the spin relaxation, while precession is included in a residual nonlinear term. We thus propose to study the stochastic dynamics of a system of soft classical spins [26] S_i^α , given by

$$\frac{\partial S_i^\alpha}{\partial t} = g \epsilon_{\alpha\beta\gamma} S_i^\beta \frac{\partial H}{\partial S_i^\gamma} - \gamma \frac{\partial H}{\partial S_i^\alpha} + \eta_i^\alpha, \quad (3)$$

where i, j denote a site on a honeycomb lattice, $\alpha, \beta = x, y, z$, and the noise term η_i^α obeys

$$\langle \eta_i^\alpha(t) \eta_j^\beta(t') \rangle = 2\gamma T \delta_{ij} \delta_{\alpha\beta} \delta(t - t'). \quad (4)$$

As described below, the unitless phenomenological parameters, γ setting the relaxation rate and g the precession rate, are chosen by comparing the dynamical correlations with the results of the LL simulation, while T is simply the temperature.

The spins are taken to be soft with mass Δ , and with a general nearest-neighbor spin interaction $K_{ij}^{\alpha\beta}$, as given by the following Hamiltonian:

$$H = \sum_{\alpha\beta} \sum_{\langle ij \rangle} K_{ij}^{\alpha\beta} S_i^\alpha S_j^\beta + \frac{\Delta}{2} \sum_{i\alpha} (S_i^\alpha)^2. \quad (5)$$

The mass Δ is an additional, temperature-dependent, phenomenological parameter which determines the average spin size $\langle S_i^2 \rangle$. Quadratic Hamiltonians of this type are suitable for studying spin dynamics in cases where there is no long-range order. We will apply this to the classical Γ model, which has macroscopic degeneracy in its ground state, preventing long-range order even at low temperatures. A similar treatment for the Kitaev model is given in the Appendix. Following a path-integral formulation of the MSR approach [27–29], we write a generating functional for dynamical correlations as

$$Z = \left\langle \int DS |M| \delta \left(\frac{\partial S_i^\alpha}{\partial t} - g \epsilon_{\alpha\beta\gamma} S_i^\beta \frac{\partial H}{\partial S_i^\gamma} + \gamma \frac{\partial H}{\partial S_j^\alpha} - \eta_i^\alpha \right) \right\rangle_\eta, \quad (6)$$

where $\langle \dots \rangle_\eta$ denotes averaging over the noise fluctuations η , and M is a Jacobian matrix. For the model we consider here we may take the determinant $|M| = 1$. Writing the δ function as an integral over \hat{S}_i^α , and averaging over η , we obtain $Z = \int D\hat{S} DS e^{-S}$ where the MSR action is given by

$$S = - \int dt \left[\hat{S}_i^\alpha (\partial_t S_i^\alpha + \gamma K_{ij}^{\alpha\beta} S_j^\beta + \gamma \Delta S_i^\alpha) + \gamma T (\hat{S}_i^\alpha)^2 - g \epsilon_{\alpha\beta\gamma} \hat{S}_i^\alpha S_i^\beta K_{ij}^{\gamma\delta} S_j^\delta \right]. \quad (7)$$

Within this formalism it is possible to calculate dynamical correlation functions, using perturbation theory in g .

Zeroth order in g . When $g = 0$, the dynamics is purely relaxational. The bare response Green's function, defined as

$$[G_0(\omega)]_{ij}^{\alpha\beta} \equiv \langle \hat{S}_i^\alpha(-\omega) S_j^\beta(\omega) \rangle_0, \quad (8)$$

is given by (its inverse)

$$[G_0^{-1}(\omega)]_{ij}^{\alpha\beta} = (-i\omega + \gamma\Delta) \delta_{\alpha\beta} \delta_{ij} + K_{ij}^{\alpha\beta}. \quad (9)$$

We will represent this diagrammatically using Fig. 8(a). Similarly, the bare correlation function is given by

$$[C_0(\omega)]_{ij}^{\alpha\beta} \equiv \langle S_i^\alpha(-\omega) S_j^\beta(\omega) \rangle_0 = 2\gamma T (G_0^\dagger(\omega) G_0(\omega))_{ij}^{\alpha\beta}. \quad (10)$$

Diagrammatically, this is represented in Fig. 8(b), where the noise vertex is represented by a dot, $\bullet = 2\gamma T$.

In the pure Γ model, which is defined by

$$K_{ij}^{\alpha\beta} = \begin{cases} \Gamma & \alpha \neq \beta \neq \langle ij \rangle \\ 0 & \text{otherwise} \end{cases}, \quad (11)$$

the classical degrees of freedom can be divided into sectors—one for each hexagon. For example, as discussed in the previous section, going around one of the white hexagons in Fig. 5, we can identify six spin components which interact only within themselves. Their dynamics is independent of the rest of the system, manifesting the macroscopic degeneracy of

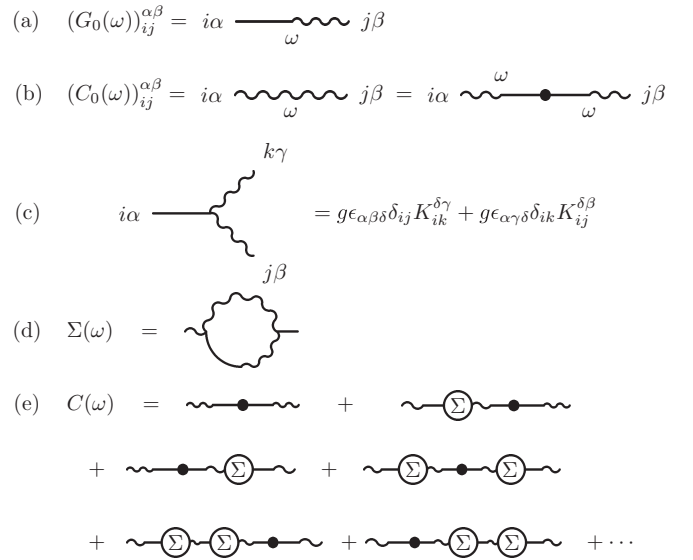


FIG. 8. Feynman diagrams for the MSR formalism: (a) bare response function, (b) bare correlation function, (c) precession vertex, (d) self-energy diagram, (e) perturbative expansion of the dressed correlation function, in powers of the self-energy Σ , see Eq. (15).

the classical system. We rename these degrees of freedom as follows,

$$\{S_1^x, S_2^y, S_3^z, S_4^x, S_5^y, S_6^z\} \equiv \{\sigma_1, \sigma_2, \sigma_3, \sigma_4, \sigma_5, \sigma_6\}. \quad (12)$$

The Hamiltonian, restricted to this sector, is given by

$$H_{\text{hexagon}} = \sum_{l=1}^6 \left(\Gamma \sigma_l \sigma_{l+1} + \frac{\Delta}{2} \sigma_l^2 \right). \quad (13)$$

The energy eigenvalues, which determine the relaxation rate, are $\varepsilon_m = 2\Gamma \cos \pi m/3 + \Delta$, $m = 1 \dots 6$. Clearly, the model is stable only for $\Delta > 2|\Gamma|$. The $g = 0$ dynamical correlation function within these six spin components is given by

$$\langle \sigma_l(\omega) \sigma_{l'}(\omega') \rangle = \frac{1}{6} \sum_{m=1}^6 \cos \left(\frac{\pi m(l-l')}{3} \right) \frac{2\gamma T 2\pi \delta(\omega + \omega')}{\omega^2 + \gamma^2 \varepsilon_m^2}, \quad (14)$$

while the correlation with spin components which do not appear in Eq. (12) is identically zero. Δ may be chosen so that $\langle \sigma_l^2 \rangle$ is a constant; at the $g = 0$ level Δ should obey $\langle \sigma_l^2 \rangle = \sum_m (T/6\varepsilon_m) = 1$. Clearly, the dynamics for $g = 0$ is purely relaxational, with a peak at $\omega = 0$. Thus, γ can be chosen such that Eq. (14) reproduces the width of the low-energy peak as obtained in the LL simulations. Focusing on the dynamic structure factor $\langle S^\alpha(\mathbf{q}, \omega) S^\alpha(-\mathbf{q}, -\omega) \rangle$, we note that for each hexagon $\langle S_l^x S_{l'}^x \rangle \neq 0$ only for $l, l' = 1, 4$, $\langle S_l^y S_{l'}^y \rangle \neq 0$ only for $l, l' = 2, 5$, and $\langle S_l^z S_{l'}^z \rangle \neq 0$ only for $l, l' = 3, 6$, in line with the symmetry consideration of the previous section and in Appendix B. In the antiferromagnetic Γ model, the lowest eigenvalue is $\varepsilon_3 = -2\Gamma + \Delta$. Noting that there are nonzero correlations only for $l - l' = 0, 3$, we find that the contribution of this eigenvalue to the spectrum at Γ vanishes, and one would expect only the higher-energy modes, i.e., faster relaxations, to contribute at this momentum. A similar argument holds for

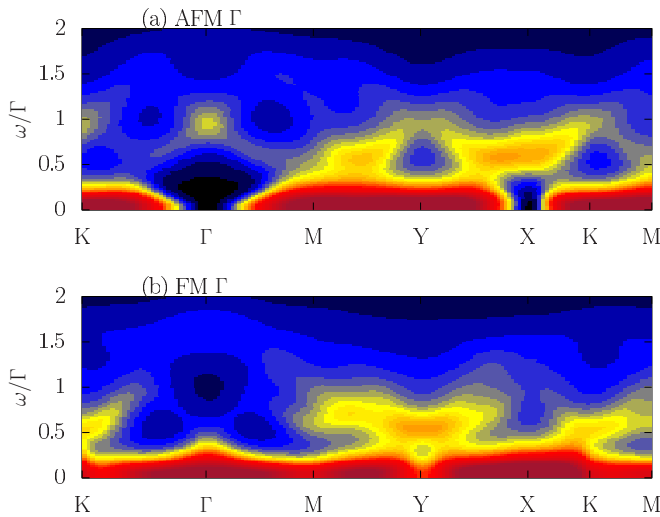


FIG. 9. Dynamic structure factor as obtained from Eq. (15), for (a) the AFM $\Gamma > 0$, and (b) the FM $\Gamma < 0$ models. Here we have used $\gamma = 0.12$, $\Delta = 2.05\Gamma$, and $g^2T = 0.04\Gamma$.

the low-energy correlations at X . Thus we find a depletion in the dynamic structure factor at Γ and X , echoing the analysis of the zero modes in the previous section.

Perturbation theory in g . It is possible to treat the precession term using diagrammatic perturbation theory. We represent the *symmetrized* precession vertex by Fig. 8(c). The dressed correlation function $C_{ij}^{\alpha\beta}(\omega)$ can be calculated approximately by summing over a subset of infinite diagrams, as shown in Fig. 8. Specifically, we approximate $C(\omega)$ by a product of two infinite series,

$$C(\omega) \approx 2\gamma T \left| G_0(\omega) \sum_{n=0}^{\infty} (\Sigma(\omega)G_0(\omega))^n \right|^2, \quad (15)$$

where the self-energy Σ is calculated to leading order in g . The self-energy term for the Γ model dynamics mixes different sectors, and therefore its calculation must be done in Fourier space. However, the procedure is no different than in quantum field theory, once the appropriate Feynman rules are determined. Figure 9 shows the resulting dynamic structure factor. Equation (14), obtained for $g = 0$, qualitatively accounts for the low-frequency features, including the depletion at Γ and X in the AFM case. The main qualitative effect of finite $g > 0$ on the dynamic structure factor is the addition of correlations peaked at finite frequency, due to the precession of the spins. In Appendix C we describe the calculation for the Kitaev model, which is simpler and can be done in real space. Furthermore, the closed-form result for the Kitaev model shows that the self-energy is larger for the mode which is suppressed at low energies. Similar behavior is observed in Fig. 9 for the Γ model, where the precession features appear at finite frequency at the same momentum positions with depleted low-energy correlations. Besides the qualitative effect of precessional dynamics, a finite g is also expected to renormalize the values of γ and Δ required to fit the numerical data obtained at a given temperature.

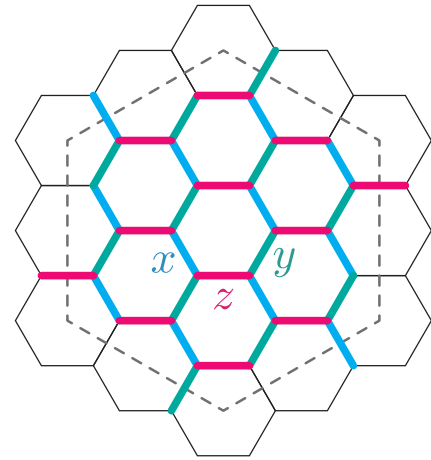


FIG. 10. Finite-size honeycomb clusters with 24 spins and periodic boundary conditions. Bonds along the three different directions are labeled as the x , y , and z bond, which are along -60° , 60° , and horizontal directions, respectively.

IV. DYNAMICS OF THE SPIN- $\frac{1}{2}$ MODEL

Using the exact-diagonalization method, described in Ref. [32] and Appendix D, we study the finite-temperature dynamical spin structure factors of the $S = 1/2$ AFM Γ model. Here we use a 24-site cluster with periodic boundary conditions, illustrated in Fig. 10. As explained below, the dynamical spin structure factor of the quantum model shows a gradual classical-to-quantum crossover when the temperature is decreased.

Before going into details of the quantum spin dynamics of the Γ model, we summarize the energy scale of the quantum $S = 1/2\Gamma$ model. As shown in Ref. [24] and Fig. 11, there are two temperature scales given by the peaks in the temperature dependence of the specific heat. The higher-temperature peak appears at around $T_2/\Gamma \approx 0.4$ and the lower-temperature peak emerges below $T_1/\Gamma \lesssim 0.03$. The two-peak structure in the temperature dependence of the specific heat has been found in the Kitaev model [6] and in the proximity of the Kitaev's spin liquid [33], although the balance of the entropy released by these two peaks is different from that of the Γ model.

In Fig. 12, the momentum dependence of the equi-energy slices of $S(\mathbf{Q}, \omega)$ are shown by changing temperature and

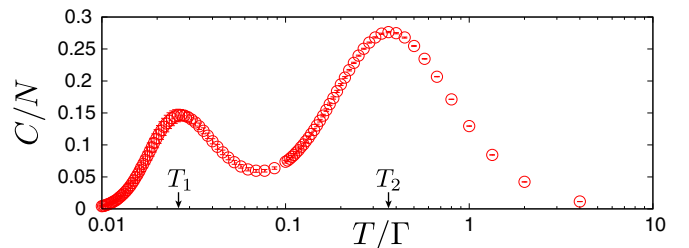


FIG. 11. Specific heat C/N of the AFM Γ model on the $N = 24$ -site cluster [24], calculated by the typical pure quantum states approach [30,31]. There are two maxima in the temperature dependence of C/N . The error bars are the standard errors estimated by 32 random initial vectors.

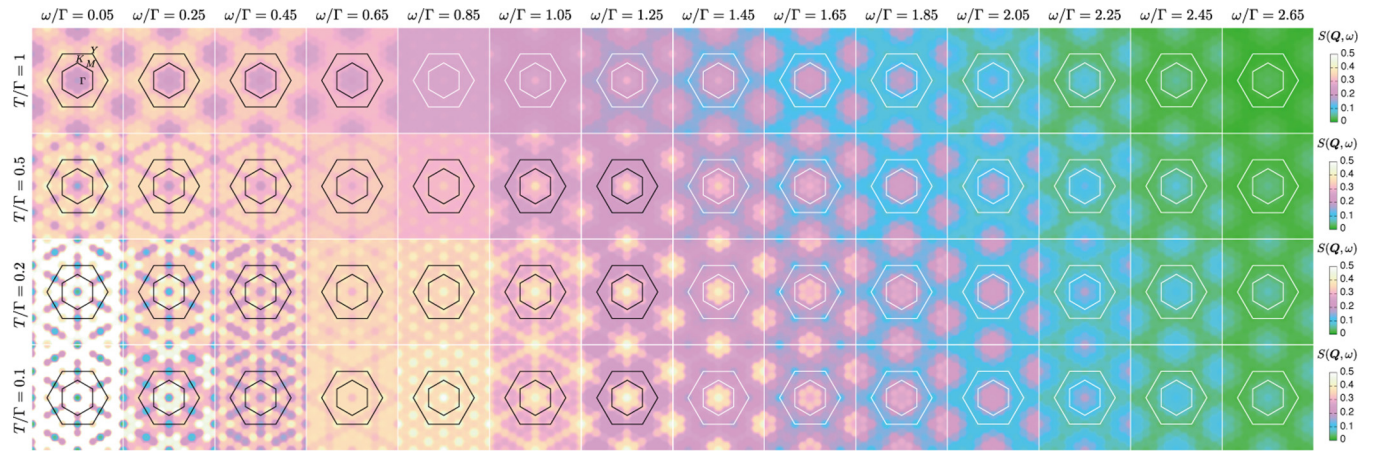


FIG. 12. Equi-energy slices of the dynamical spin structure factors of the $\Gamma > 0$ model. The momentum dependence of the equi-energy slices is shown by changing temperature and frequency. From the top row to the bottom row, the equi-energy slices of the dynamical spin structure factors are shown at $T/\Gamma = 1, 0.5, 0.2,$ and 0.1 . The equi-energy slices are prepared by averaging the spectra within an energy window whose width is 0.1 . For visibility, the dynamical spin structure factors at discrete momenta obtained by the simulation are interpolated. Here, the broadening factor $\eta/\Gamma = 0.02$ is used (see Appendix D for the definition of η).

frequency. The equi-energy slices are prepared by averaging the spectra within an energy window whose width is 0.1 . The momentum dependence is numerically interpolated for visibility without changing the simulation results at the discrete momenta \mathbf{Q} compatible with the finite-size cluster. At $T/\Gamma = 1 > T_2/\Gamma \approx 0.4$, almost momentum-independent behaviors of $S(\mathbf{Q}, \omega)$ are found except around the Γ point, where spectral weight is suppressed for $\omega/\Gamma < 1$ and is shifted to the high-energy region $\omega/\Gamma > 1$. Below $T/\Gamma = 0.5 \approx T_2/\Gamma$, the suppression of the low-energy spectral weight (or relaxational dynamics) at Γ and X points becomes notable, which is consistent with the classical dynamics.

To examine the temperature dependence of the low-energy spectral weight, we show the temperature evolution of $S(\mathbf{Q} = \Gamma, \omega)$ in comparison with $S(\mathbf{Q} = M, \omega)$ in Fig. 13. Below the high-temperature scale $T/\Gamma \approx 0.4$, $S(\mathbf{Q} = \Gamma, \omega)$ shows reduced spectral weight in the low-energy region below $\omega/\Gamma \approx 0.5$, while $S(\mathbf{Q} = M, \omega)$ shows substantial spectral weight in the low-energy region. We further note that the Fourier transformation of $S(\mathbf{Q}, \omega)$, $S(\mathbf{r}_{\ell m}, \omega)$, also satisfies the symmetry properties at finite temperatures, as discussed in Sec. II.

For closer comparison with the classical dynamics, we show $S(\mathbf{Q}, \omega)$ at $T/\Gamma = 0.5, 0.2, 0.1,$ and 0 along symmetry lines in Fig. 14. In addition to the suppression of the low-energy spectral weight at Γ and X points, which is in common with the classical spin dynamics, the low-energy spectral weight for $\omega/\Gamma \lesssim 0.5$ decreases at K and Y upon cooling. This suppression at the K and Y points is characteristic of the $S = 1/2 \Gamma$ model.

To gain insight into the difference between the quantum and classical dynamics at the K and Y points, we examine the static spin-spin correlation function at zero temperature. In Fig. 15, $\langle S_0^\alpha S_r^\beta \rangle$ ($\alpha, \beta = x, y, z$) are shown in the 24-site cluster with the periodic boundary condition. These correlators in the quantum model are very similar to the static correlation functions of the classical model, as shown in Fig. 4. Due to the symmetry of the Γ model, the static spin-spin correlation functions are zero for

many spin pairs. However, there are differences among them: For example, there exist finite nearest-neighbor correlations $\langle S_0^\alpha S_r^\beta \rangle$ ($\alpha, \beta = x, y, z$) for $\alpha = \beta$ and the additional second-nearest-neighbor correlations for $\alpha \neq \beta$. The fact that these correlations are finite, while they are absent in the classical limit, indicates that quantum fluctuations are important even when $T > T_1$.

The most significant difference is the nearest-neighbor correlations for $\alpha = \beta$, which are zero in the classical model due to the local symmetry discussed in Sec. II. The nearest-neighbor ferromagnetic correlations in the real space hinder

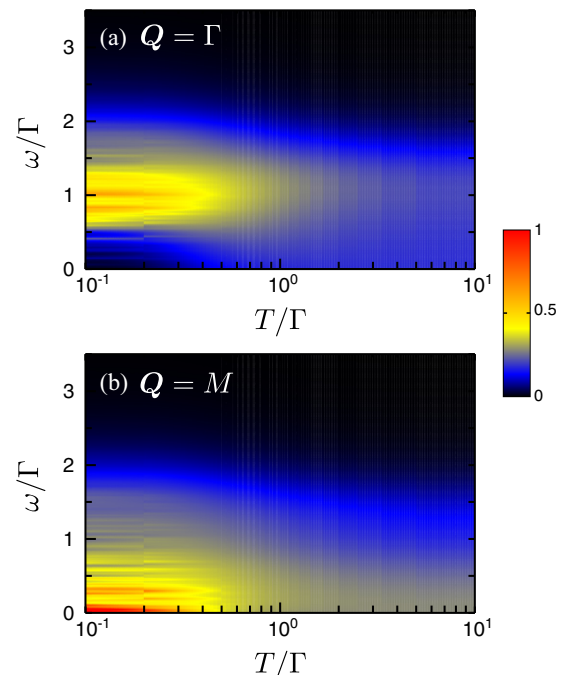


FIG. 13. Temperature evolution of $S(\mathbf{Q} = \Gamma, \omega)$ and $S(\mathbf{Q} = M, \omega)$ for the $\Gamma > 0$ model.

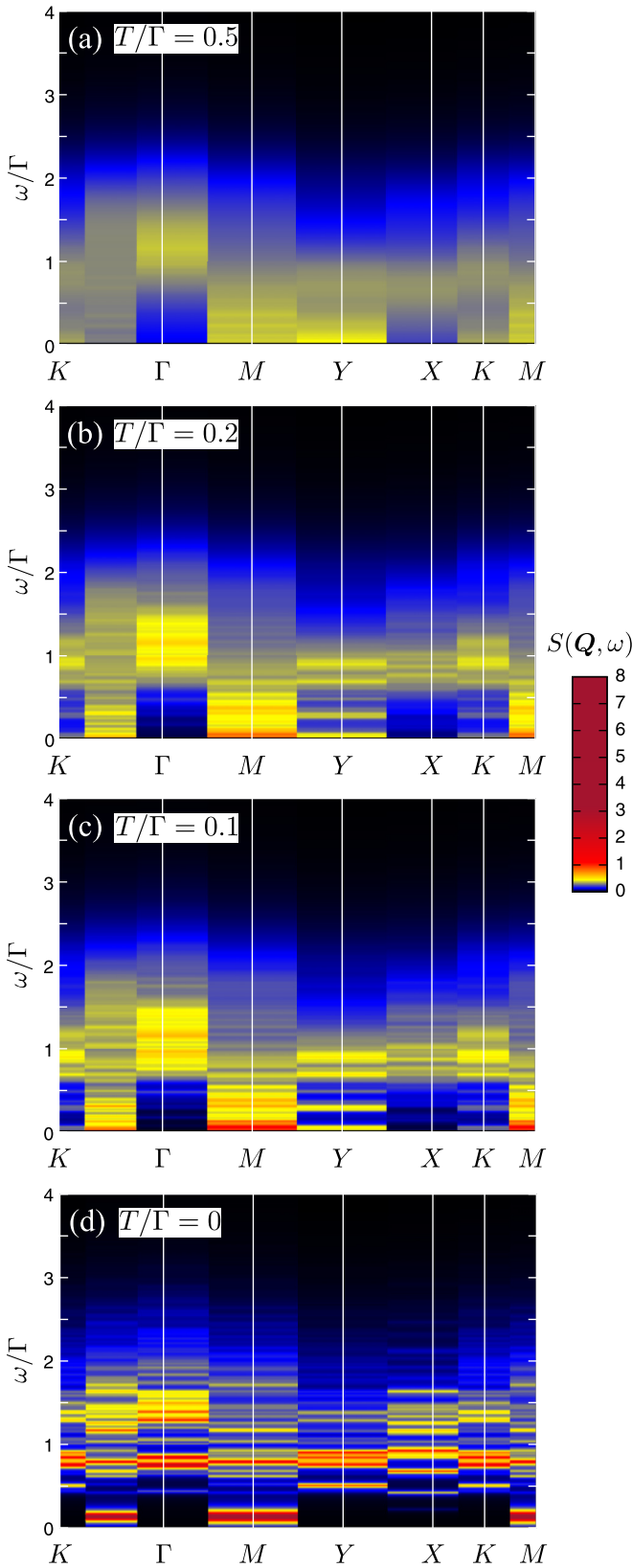


FIG. 14. Dynamical spin structure factors of the $S = 1/2$ AFM Γ model at (a) $T = 0.5$, (b) $T = 0.2$, (c) $T = 0.1$, and (d) $T = 0$, along symmetry lines. For visibility, the broadening factor $\eta/\Gamma = 0.02$ is used (see Appendix D for the definition of η).

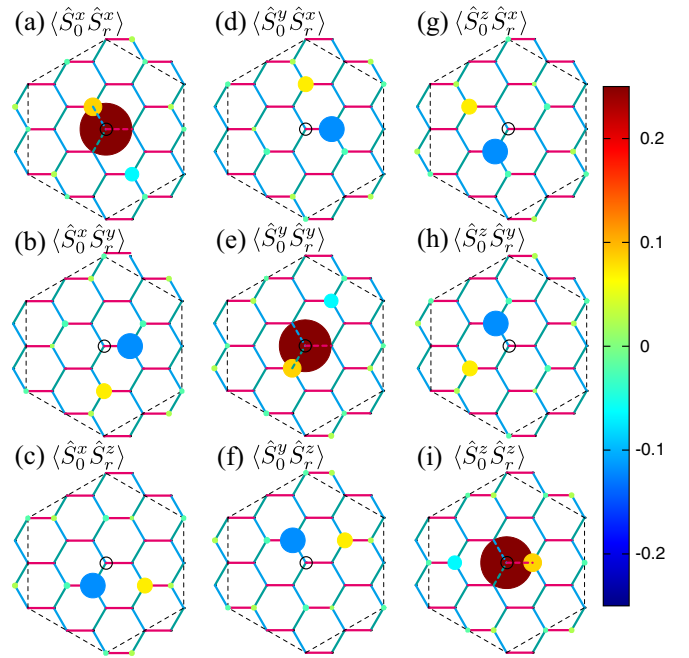


FIG. 15. Real-space static spin-spin correlation function, $\langle S_0^\alpha S_r^\beta \rangle$ ($\alpha, \beta = x, y, z$), of the $S = 1/2$ $\Gamma > 0$ model on the 24-site cluster with periodic boundary conditions, at $T = 0$. The location of the origin 0 is denoted by the open circle (\circ). The radiuses of the closed circles at r represent the amplitude of $|\langle S_0^\alpha S_r^\beta \rangle|$, while the color of the closed circles shows $\langle S_0^\alpha S_r^\beta \rangle$. Within numerical accuracy, there is no spin-spin correlation represented by a circle with a radius smaller than the width of the solid lines representing the bonds.

the antiferromagnetic low-energy fluctuations at the Y and K points in the momentum space. As a result, these correlations harden the spin fluctuations at these momenta. In other words, these correlations suppress the relaxational dynamics and introduce the quasicollective precessional dynamics at these momenta.

A quantitative description of the classical-quantum crossover is obtained by examining the temperature dependence of the typical static spin-spin correlation functions shown in Fig. 16. While the off-diagonal nearest-neighbor correlations $\langle S_0^\alpha S_r^\beta \rangle$ on the γ bond, where (α, β, γ) is a

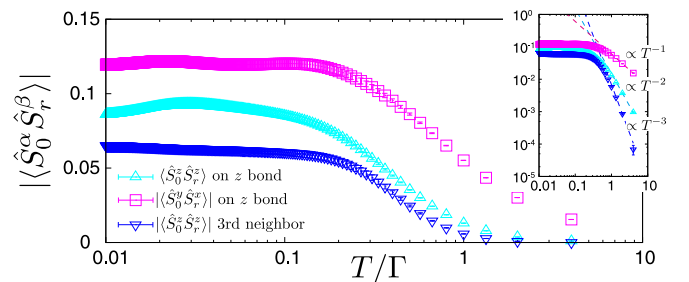


FIG. 16. Temperature dependence of static spin-spin correlations of the AFM Γ model on the 24-site cluster. Here, the error bars, which are smaller than or comparable to the symbol size, are the standard errors estimated by several random initial vectors.

permutation of (x, y, z) , are dominant at temperatures above and around $T_2/\Gamma \approx 0.4$, the diagonal nearest-neighbor correlations $\langle S_0^\alpha S_r^\alpha \rangle$ start to saturate upon cooling for $T < T_2$. Therefore, the classical precessional dynamics due to the off-diagonal nearest-neighbor correlations governs the dynamics for $T \gtrsim T_2$. On the other hand, the emergent quantum dynamics is generated by the diagonal nearest-neighbor correlations for $T < T_2$. Here, we note that dominance of the off-diagonal nearest-neighbor correlations originates from their Curie-like temperature dependence in the high-temperature region, which is evident in the inset of Fig. 16, while temperature dependence of the diagonal nearest-neighbor and third-nearest-neighbor correlations shows T^{-2} and T^{-3} scaling, respectively. In Appendix E we show how these power-law behaviors can be obtained using a high-temperature expansion.

V. DISCUSSION

In this work, we investigated classical and quantum dynamics of the Γ model, the bond-dependent symmetric and anisotropic spin interaction on the honeycomb lattice. Such exchange interaction arises in strongly spin-orbit-coupled Mott insulators, in addition to the usual Heisenberg and Kitaev (the bond-dependent Ising) interactions [7,14]. There exist a number of so-called ‘‘Kitaev materials,’’ such as α, β, γ -Li₂IrO₃ and α -RuCl₃, where the Kitaev interaction, if dominant, may lead to a quantum spin liquid phase. However, the strength of the Γ interaction can be as large as that of the Kitaev interaction, especially in the case of α -RuCl₃, according to recent *ab initio* computations [15]. The presence of other interactions has been regarded as an obstacle for realizing the quantum spin liquid ground state in this class of materials.

On the other hand, the Γ interaction is also highly frustrated at the classical level, just like the Kitaev model. Given that the strength of this interaction is significant in some materials, the nature of the quantum ground state of the Γ model is highly relevant for the interpretation of the experiments. In the case of α -RuCl₃, for example, it has been speculated that the scattering continuum seen in recent neutron-scattering experiments may come from a nearby quantum spin liquid, even though the actual ground state is a magnetically ordered state [34,35]. The magnetic order can be suppressed by an external in-plane magnetic field, and the resulting paramagnetic state is speculated to be a field-induced quantum spin liquid [18,20,21]. Currently it is highly debated whether the Kitaev interaction or other interactions or both could be responsible for the formation of a putative quantum spin liquid ground state.

In the present work, we focused on the Γ interaction and pointed out the similarity to the Kitaev model in the correspondence between classical and quantum dynamics. We showed that the zero mode structure of the highly degenerate manifold of the classical ground states is reflected in the classical dynamical spin structure factor. In addition, we clarified different roles of relaxational and precessional dynamics in the dynamical spin structure factor of the classical model. Remarkably, this feature survives in the quantum model down to very-low-energy scales. This would imply that the full degenerate manifold of the classical states is participating in quantum fluctuations down to very-low-energy scales. This situation resembles the results of the Kitaev model, obtained

in a previous study [2], where the quantum dynamical spin structure factor is qualitatively similar to the classical results down to low energies above the small flux gap in the underlying spin liquid ground state. This correspondence in the Kitaev model was apparent even in the temperature/energy window where the underlying low-energy degrees of freedom are Majorana fermions, not the semiclassical spins. Since the quantum Γ model is not exactly solvable, we do not know the true quantum ground state at zero temperature. It has been suggested that order by quantum disorder leads to a symmetry-broken state [8]. The resemblance to the Kitaev model, however, suggests that the quantum ground state of the Γ model may also be a quantum spin liquid, which results from the ‘‘collapse’’ of the degenerate classical manifold. Such a conclusion may also be consistent with a recent density-matrix renormalization group computation of the same model [25], where the ground seems to be a highly correlated quantum paramagnet. If the Γ model can indeed support a quantum spin liquid ground state, the presence of this interaction in real materials may not necessarily be an obstruction for the realization of the quantum spin liquid ground state. The firm answer to this question would require further studies of the quantum and classical models with both the Kitaev and Γ interactions.

ACKNOWLEDGMENTS

Work at ORNL is supported by the US Department of Energy (DOE), Office of Science, Basic Energy Sciences, Scientific User Facilities Division. C.D.B. acknowledges support from the Los Alamos National Laboratory LDRD program. G.W. and Y.B.K. are supported by NSERC of Canada and the Center for Quantum Materials at the University of Toronto. G.W. was additionally supported by the Israel Science Foundation (Grant No. 585/13). Y.Y. was supported by JSPS KAKENHI (Grant No. 16H06345) and was supported by PRESTO, JST (JPMJPR15NF). This research was supported by MEXT as ‘‘Priority Issue on Post-K Computers’’ (Creation of New Functional Devices and High-Performance Materials to Support Next-Generation Industries) and ‘‘Exploratory Challenge on Post-K Computers’’ (Frontiers of Basic Science: Challenging the Limits). Our numerical calculation was partly carried out at the Supercomputer Center, Institute for Solid State Physics, University of Tokyo. The exact diagonalization (ED) calculations are partly double-checked by using an open-source ED program package $\mathcal{H}\Phi$ [36,37].

APPENDIX A: ZERO MODE STRUCTURE

The momentum space distribution of the zero modes can be derived from the set of constraints satisfied by the ground-state manifold. As reported by Rouschatzakis and Perkins [8], the classical ground state of the AFM Γ model satisfies the following constraints on each bond of the lattice:

$$\begin{aligned} S_1^x &= -S_2^y, & \text{and} & & S_1^y &= -S_2^x & \text{for } z \text{ bonds,} \\ S_1^x &= -S_2^z, & \text{and} & & S_1^z &= -S_2^x & \text{for } y \text{ bonds,} \\ S_1^y &= -S_2^z, & \text{and} & & S_1^z &= -S_2^y & \text{for } x \text{ bonds,} \end{aligned} \quad (\text{A1})$$

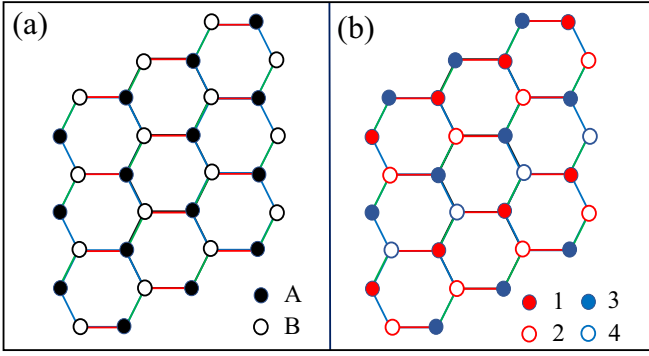


FIG. 17. (a) Two-sublattice decomposition of the honeycomb lattice. (b) Four-sublattice decomposition of the honeycomb lattice.

where 1 and 2 denote the two sites on the given bond. Equation (A2) implies that the following identities hold for any ground-state configuration:

$$\begin{aligned} S_A^x &= -S_B^y, & S_A^y &= -S_B^x, & S_A^z &= -S_B^z, \\ S_A^z &= -S_B^x, & S_A^x &= -S_B^z, & S_A^y &= -S_B^y, \end{aligned} \quad (\text{A2})$$

where $S_A^\mu = \sum_{j \in A} S_j^\mu$ and $S_B^\mu = \sum_{j \in B} S_j^\mu$ and (A, B) denote the two sublattices of the honeycomb lattice shown in Fig. 17(a). The conditions (A2) lead to $S_A^x = S_A^y = S_A^z$, $S_B^x = S_B^y = S_B^z$, and $S_A^\mu + S_B^\mu = 0$, implying that the ground states of the classical AFM Γ model have no zero-momentum component. This simple analysis proves the absence of elastic ($\omega = 0$) spectral weight at the Γ point.

Our next goal is to demonstrate the absence of elastic weight at the X points. For this purpose, we divide the honeycomb lattice into four sublattices, as shown in Fig. 17(b). Without loss of generality, we prove the statement for one of the three X points, say X_1 . The C_6 symmetry of the honeycomb lattice guarantees that the result is the same for X_2 and X_3 . The X_1 component of a given spin configuration is

$$S_{X_1}^\mu = \frac{2}{\sqrt{N}} [S_1^\mu + S_2^\mu - S_3^\mu - S_4^\mu], \quad (\text{A3})$$

where $S_r^\mu = \sum_{j \in r} S_j^\mu$ and the integer index $1 \leq r \leq 4$ denotes each of the six sublattices and N is the total number of sites. From the general ground-state condition (A2), we obtain

$$\begin{aligned} S_1^y &= -S_2^z, & S_1^z &= -S_2^y, & S_1^x &= -S_4^y, \\ S_1^y &= -S_4^x, & S_1^z &= -S_4^x, & S_1^x &= -S_4^z, \\ S_2^x &= -S_3^y, & S_2^y &= -S_3^x, & S_2^z &= -S_3^z, \\ S_2^z &= -S_3^x, & S_3^y &= -S_4^z, & S_3^z &= -S_4^y. \end{aligned} \quad (\text{A4})$$

These identities give $S_1^x = -S_4^y = S_3^z = S_2^x$, $S_3^x = -S_2^y = S_1^z = -S_4^x$, implying that $S_{X_1}^x = 0$. Similarly, Eq. (A4) leads to $S_1^y = -S_2^z = S_3^x = -S_4^y$, $S_1^y = -S_4^x = S_1^z = -S_2^z$, $S_3^z = -S_4^y = S_1^x = -S_4^z$, implying that $S_{X_1}^y = S_{X_1}^z = 0$. In other words, the ground-state configurations of the AFM Γ model have no Γ or X_μ ($\mu = 1, 2, 3$) components, implying the absence of elastic ($\omega = 0$) spectral weight at any of those wave vectors.

APPENDIX B: SYMMETRY ANALYSIS OF $S^{\alpha\beta}(\mathbf{r}, \mathbf{r}', \omega)$

Here we derive selection rules of the real-space dynamical spin structure factor of \mathcal{H} for arbitrary spin S . For this purpose, we introduce the six-sublattice decomposition of the honeycomb lattice that is depicted in Fig. 5 [8]. We demonstrate that six out of the nine components of the real-space and real-time magnetic structure factor,

$$S^{\alpha\beta}(\mathbf{r}, \mathbf{r}', t) = \langle S_r^\alpha(0) S_{r'}^\beta(t) \rangle, \quad (\text{B1})$$

always vanish as a consequence of the Hamiltonian symmetries that we discuss next.

It was noticed in Ref. [8] that the Γ model (1) is invariant under a set of three spin transformations acting on each of the six sublattices depicted in Fig. 5.

(1) If we decompose the full lattice into the white hexagons shown in Fig. 5, the Hamiltonian \mathcal{H} is invariant under the symmetry operation

$$\mathcal{R}_a = \prod_{i \in \{1,4\}} C_{2x}(i) \prod_{i' \in \{2,5\}} C_{2y}(i') \prod_{i'' \in \{3,6\}} C_{2z}(i''). \quad (\text{B2})$$

(2) Similarly, a lattice decomposition into the dark-gray hexagons shown in Fig. 5 reveals the symmetry operation

$$\mathcal{R}_b = \prod_{i \in \{6,5\}} C_{2x}(i) \prod_{i' \in \{3,4\}} C_{2y}(i') \prod_{i'' \in \{1,2\}} C_{2z}(i''). \quad (\text{B3})$$

(3) Finally, a decomposition into the light-gray hexagons in Fig. 5 leads to the symmetry operation

$$\mathcal{R}_c = \prod_{i \in \{2,3\}} C_{2x}(i) \prod_{i' \in \{1,6\}} C_{2y}(i') \prod_{i'' \in \{4,5\}} C_{2z}(i''). \quad (\text{B4})$$

We will derive now selection rules based on these symmetries. Given that these selection rules are exactly the same for any pair of sites \mathbf{r} and \mathbf{r}' belonging to a given pair of sublattices ν and ν' , we will use the notation $\langle S_\nu^\alpha(0) S_{\nu'}^\beta(t) \rangle$ instead of $\langle S_r^\alpha(0) S_{r'}^\beta(t) \rangle$. We start by considering spin-spin correlators between sites on the same sublattice, i.e., both \mathbf{r} and \mathbf{r}' belong to the same sublattice ν ($1 \leq \nu \leq 6$). Off-diagonal contributions involve a product of two different spin components S_ν^α and S_ν^β with $\alpha \neq \beta$. Because both spin operators belong to the same sublattice, they rotate about the same axis under the transformations \mathcal{R}_a , \mathcal{R}_b , or \mathcal{R}_c . We can always choose the transformation \mathcal{R}_η that corresponds to a π rotation about the α axis. Given that α and β are different components, we have

$$\mathcal{R}_\eta^\dagger S_\nu^\alpha \mathcal{R}_\eta = S_\nu^\alpha, \quad \text{and} \quad \mathcal{R}_\eta^\dagger S_\nu^\beta \mathcal{R}_\eta = -S_\nu^\beta, \quad (\text{B5})$$

implying that

$$\begin{aligned} \langle S_\nu^\alpha(0) S_\nu^\beta(t) \rangle &= \text{Tr} [e^{-(\mathcal{H}/k_B T)} S_\nu^\alpha(0) S_\nu^\beta(t)] \\ &= \text{Tr} [\mathcal{R}_\eta^\dagger e^{-(\mathcal{H}/k_B T)} S_\nu^\alpha(0) S_\nu^\beta(t) \mathcal{R}_\eta] \\ &= \text{Tr} [e^{-(\mathcal{H}/k_B T)} \mathcal{R}_\eta^\dagger S_\nu^\alpha(0) \mathcal{R}_\eta \mathcal{R}_\eta^\dagger S_\nu^\beta(t) \mathcal{R}_\eta] \\ &= -\langle S_\nu^\alpha(0) S_\nu^\beta(t) \rangle = 0. \end{aligned} \quad (\text{B6})$$

By using this result and from the Hamiltonian symmetry under the product of a spin rotation by $2\pi/3$ about the [111] direction and an orbital rotation by the same angle along the direction

perpendicular to the plane of the honeycomb lattice, we obtain

$$\langle S_v^\alpha(0)S_v^\beta(t) \rangle = \delta_{\alpha\beta} \langle S_v^z(0)S_v^z(t) \rangle \quad (\text{B7})$$

for general values of α and β .

We consider now the spin-spin correlator (B1) for \mathbf{r} and \mathbf{r}' belonging to *different* sublattices with the *same parity* ($v \neq v'$ and $v + v'$ even). For any diagonal component ($\mu = \nu$), it is easy to verify that at least one of the three symmetry transformations, \mathcal{R}_a , \mathcal{R}_b , or \mathcal{R}_c , changes the sign of only one of the two spin operators:

$$\mathcal{R}_\eta^\dagger S_\nu^\alpha \mathcal{R}_\eta = \pm S_\nu^\alpha, \quad \text{and} \quad \mathcal{R}_\eta^\dagger S_{\nu'}^\alpha \mathcal{R}_\eta = \mp S_{\nu'}^\alpha. \quad (\text{B8})$$

Here $\eta = a, b$, or c denotes the transformation that satisfies (B8). Note that $\mathcal{R}_\eta^\dagger = \mathcal{R}_\eta$. Once again, following the same procedure as in Eq. (B6), we obtain

$$\langle S_v^\alpha(0)S_{v'}^\alpha(t) \rangle = 0. \quad (\text{B9})$$

By using a similar procedure, we can demonstrate that three, out of the six, off-diagonal correlators between different sublattices with the same parity are also equal to zero:

$$\begin{aligned} \langle S_1^x(0)S_3^y(t) \rangle &= \langle S_1^y(0)S_3^z(t) \rangle = \langle S_1^z(0)S_3^x(t) \rangle = 0, \\ \langle S_1^x(0)S_5^z(t) \rangle &= \langle S_1^z(0)S_5^y(t) \rangle = \langle S_1^y(0)S_5^x(t) \rangle = 0, \\ \langle S_2^y(0)S_4^z(t) \rangle &= \langle S_2^z(0)S_4^x(t) \rangle = \langle S_2^x(0)S_4^y(t) \rangle = 0, \\ \langle S_2^y(0)S_6^x(t) \rangle &= \langle S_2^x(0)S_6^z(t) \rangle = \langle S_2^z(0)S_6^y(t) \rangle = 0. \end{aligned} \quad (\text{B10})$$

We note that $\langle S_r^\alpha(0)S_{r'}^\beta(t) \rangle = 0$ implies $\langle S_{r'}^\beta(0)S_r^\alpha(t) \rangle = 0$.

Similarly, using the symmetries \mathcal{R}_a , \mathcal{R}_b , and \mathcal{R}_c , we can demonstrate that

$$\begin{aligned} \langle S_1^x(0)S_6^x(t) \rangle &= \langle S_1^z(0)S_6^z(t) \rangle = \langle S_1^x(0)S_6^y(t) \rangle \\ &= \langle S_1^y(0)S_6^x(t) \rangle = \langle S_1^z(0)S_6^y(t) \rangle \\ &= \langle S_1^y(0)S_6^z(t) \rangle = 0, \\ \langle S_1^x(0)S_2^x(t) \rangle &= \langle S_1^y(0)S_2^y(t) \rangle = \langle S_1^x(0)S_2^z(t) \rangle \\ &= \langle S_1^z(0)S_2^x(t) \rangle = \langle S_1^z(0)S_2^y(t) \rangle \\ &= \langle S_1^y(0)S_2^z(t) \rangle = 0, \\ \langle S_1^y(0)S_4^y(t) \rangle &= \langle S_1^z(0)S_4^z(t) \rangle = \langle S_1^x(0)S_4^x(t) \rangle \\ &= \langle S_1^z(0)S_4^x(t) \rangle = \langle S_1^x(0)S_4^y(t) \rangle \\ &= \langle S_1^y(0)S_4^x(t) \rangle = 0, \\ \langle S_2^x(0)S_1^x(t) \rangle &= \langle S_2^y(0)S_1^y(t) \rangle = \langle S_2^x(0)S_1^z(t) \rangle \\ &= \langle S_2^z(0)S_1^x(t) \rangle = \langle S_2^z(0)S_1^y(t) \rangle \\ &= \langle S_2^y(0)S_1^z(t) \rangle = 0, \\ \langle S_2^y(0)S_3^y(t) \rangle &= \langle S_2^z(0)S_3^z(t) \rangle = \langle S_2^x(0)S_3^z(t) \rangle \\ &= \langle S_2^z(0)S_3^x(t) \rangle = \langle S_2^x(0)S_3^y(t) \rangle \\ &= \langle S_2^y(0)S_3^x(t) \rangle = 0, \\ \langle S_2^x(0)S_5^x(t) \rangle &= \langle S_2^z(0)S_5^z(t) \rangle = \langle S_2^x(0)S_5^y(t) \rangle \\ &= \langle S_2^y(0)S_5^x(t) \rangle = \langle S_2^z(0)S_5^y(t) \rangle \\ &= \langle S_2^y(0)S_5^z(t) \rangle = 0, \\ \langle S_6^x(0)S_5^x(t) \rangle &= \langle S_6^z(0)S_5^z(t) \rangle = \langle S_6^x(0)S_5^y(t) \rangle \\ &= \langle S_6^y(0)S_5^x(t) \rangle = 0. \end{aligned} \quad (\text{B11})$$

It is clear then that the symmetries \mathcal{R}_a , \mathcal{R}_b , and \mathcal{R}_c constrain six components of the real-space spin structure factor to be identically zero. The six components that vanish depend on the two sublattices to which the vectors \mathbf{r} and \mathbf{r}' belong to.

APPENDIX C: MSR TREATMENT OF THE CLASSICAL KITAEV MODEL

In the honeycomb Kitaev model, defined by

$$K_{ij}^{\alpha\beta} = \begin{cases} K & \alpha = \beta = \langle ij \rangle, \\ 0 & \text{otherwise} \end{cases}, \quad (\text{C1})$$

each component of a given spin is correlated with only one component of one neighboring spin—the one it interacts with. Thus,

$$(G_0^{-1})_{ij}^{\alpha\beta} = \begin{cases} -i\omega + \gamma\Delta & \alpha = \beta, i = j \\ \gamma K & \alpha = \beta = \langle ij \rangle, \\ 0 & \text{otherwise} \end{cases}, \quad (\text{C2})$$

from which we find that C_0 becomes a 2×2 matrix, given by

$$C_0(\omega) = \frac{1}{2} \sum_{m=\pm} \begin{pmatrix} 1 & m \\ m & 1 \end{pmatrix} \frac{1}{\omega^2 + \gamma^2(\Delta + mK)^2}. \quad (\text{C3})$$

Physically, this indicates that correlations decay at two characteristic rates, as given by the two eigenvalues $\gamma(\Delta \pm K)$. The dynamic structure factor is obtained by taking the Fourier transform, $S(\mathbf{q}, \omega) = 3C_{11}(\omega) + \sum_{\delta} e^{i\mathbf{q}\cdot\delta} C_{12}(\omega)$, where δ denotes the vectors connecting nearest neighbors. Evidently, for the antiferromagnetic Kitaev model, correlations at $\mathbf{q} = 0$ decay only at the fast rate, $\gamma(\Delta + K)$, leading to a depletion in the dynamic structure factor at low frequencies.

At finite $g > 0$, the infinite series in Eq. (15) becomes a 2×2 matrix equation, with

$$G_0(\omega) = \begin{pmatrix} -i\omega + \gamma\Delta & \gamma K \\ \gamma K & -i\omega + \gamma\Delta \end{pmatrix}^{-1}, \quad (\text{C4})$$

while the self-energy calculation yields

$$\Sigma(\omega) = -g^2 K^2 \frac{1}{-i\omega + 2\gamma\Delta} \frac{T}{\Delta^2 - K^2} \begin{pmatrix} \Delta & K \\ K & \Delta \end{pmatrix}. \quad (\text{C5})$$

Using Eq. (15), we obtain

$$\begin{aligned} C(\omega) &\approx \frac{1}{2} \sum_{m=\pm 1} \begin{pmatrix} 1 & m \\ m & 1 \end{pmatrix} \\ &\times \frac{2\gamma T}{\left| -i\omega + \gamma(\Delta + mK) + \frac{g^2 K^2 T}{\Delta^2 - K^2} \frac{\Delta + mK}{-i\omega + 2\gamma\Delta} \right|^2}. \end{aligned} \quad (\text{C6})$$

We obtain the dynamic structure factor by Fourier transforming this result (see Fig. 18). Note, for example, that only the $m = 1$ term contributes to the dynamic structure factor at $\mathbf{q} = 0$, which is suppressed at low frequencies for the AFM Kitaev, $K > 0$. Evidently, the self-energy, Eq. (C5), is larger for $m = 1$, producing a precession peak at finite ω , where the low-frequency correlations are suppressed.

APPENDIX D: DETAILS OF THE ED CALCULATION

When every eigenvalue $\{E_\nu\}$ and eigenvector $\{|\nu\rangle\}$ of the Hamiltonian \mathcal{H} are known, the Green's function at a finite

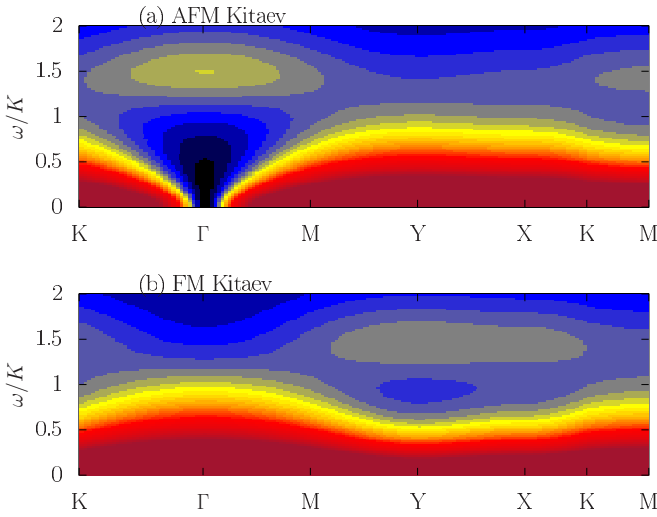


FIG. 18. Dynamic structure factor as obtained in Eq. (C6), for (a) the AFM Kitaev $K > 0$ and (b) the FM Kitaev $K < 0$ models. Here we used $\gamma = 0.25$, $\Delta = 1.05K$, and $g^2T = 0.1K$.

temperature β^{-1} is given as

$$\mathcal{G}_\beta^{AB}(\omega) = \sum_{\nu, \mu} \frac{e^{-\beta E_\nu}}{Z(\beta)} \frac{\langle \nu | A^\dagger | \mu \rangle \langle \mu | B | \nu \rangle}{\omega + i\eta + E_\nu - E_\mu}, \quad (\text{D1})$$

where Z is the partition function of the system defined as $Z(\beta) = \sum_\nu e^{-\beta E_\nu}$. For later use, we rewrite the above expression of \mathcal{G}_β^{AB} as

$$\mathcal{G}_\beta^{AB}(\omega) = \sum_\nu \frac{e^{-\beta E_\nu}}{Z(\beta)} \langle \nu | A^\dagger \frac{1}{\omega + i\eta + E_\nu - \mathcal{H}} B | \nu \rangle. \quad (\text{D2})$$

Here, we reformulate Eq. (D2) with a typical pure state [30,31,38–42] $|\psi_\beta\rangle$ to avoid using the whole set of E_ν and $|\nu\rangle$. First, we note that the normalized typical state is naively expected to behave as

$$|\psi_\beta\rangle \approx \sum_\nu e^{i\varphi_\nu} \frac{e^{-\frac{\beta}{2} E_\nu}}{\sqrt{Z(\beta)}} |\nu\rangle, \quad (\text{D3})$$

where $\varphi_\nu \in [0, 2\pi)$ are random numbers. By introducing a projection operator,

$$\hat{P}_\nu = |\nu\rangle\langle\nu|, \quad (\text{D4})$$

we rewrite the formula based on a canonical ensemble, Eq. (D2), as

$$\mathcal{G}_\beta^{AB}(\zeta) \approx \sum_\nu \langle \psi_\beta | \hat{P}_\nu A^\dagger \frac{1}{\zeta + E_\nu - \mathcal{H}} B \hat{P}_\nu | \psi_\beta \rangle. \quad (\text{D5})$$

Thus far, the exact projection operator \hat{P}_ν requires the whole set of $|\nu\rangle$.

The important step is to find an efficient implementation of the projection operator \hat{P}_ν . Although there is no $\mathcal{O}(N_F)$ implementation of the exact \hat{P}_ν in the literature as far as we know, where N_F is the dimension of the Fock space, there is a filter operator [43–46] that constructs equi-energy shells and is realizable with the numerical cost of $\mathcal{O}(N_F)$ by employing the shifted Krylov method [47], as follows.

The filter operator [43] is defined by integrating the resolvent of \hat{H} along a contour $C_{\gamma, \rho}$ defined by $z = \rho e^{i\theta} + \gamma$ with $0 \leq \theta < 2\pi$ as

$$\hat{P}_{\gamma, \rho} = \frac{1}{2\pi i} \oint_{C_{\gamma, \rho}} \frac{dz}{z - \mathcal{H}}. \quad (\text{D6})$$

If the filter operator is applied to an arbitrary wave function $|\phi\rangle = \sum_\nu d_\nu |\nu\rangle$, the operator filters the eigenvectors with the eigenvalues $E_\nu \notin (\gamma - \rho, \gamma + \rho)$. When a small γ limit is taken, the filter operator realizes a microcanonical ensemble. The filter operator is practically implemented as a Riemann sum [44,45]. The discretized filter operator is defined as

$$\hat{P}_{\gamma, \rho, M} = \frac{1}{M} \sum_{j=1}^M \frac{\rho e^{i\theta_j}}{\rho e^{i\theta_j} + \gamma - \mathcal{H}}, \quad (\text{D7})$$

where $\theta_j = 2\pi(j - 1/2)/M$. Multiplication of $\hat{P}_{\gamma, \rho, M}$ to a wave function is simply realized by the shifted Krylov subspace method, while it is hardly achievable by the standard Lanczos algorithm.

By introducing an appropriate energy grid measured from the low-energy onset E_b in energy axis,

$$\mathcal{E}_m = E_b + (2m + 1)\epsilon, \quad (\text{D8})$$

the set of the filter operators $\{\hat{P}_{\mathcal{E}_m, \epsilon, M}\}$ with the discretization parameters,

$$\delta = (E_b, \epsilon, M), \quad (\text{D9})$$

indeed replace the projection operators $\{\hat{P}_\nu\}$. The filtered typical state given by

$$|\phi_{\beta, \delta}^m\rangle = \hat{P}_{\mathcal{E}_m, \epsilon, M} |\phi_\beta\rangle \quad (\text{D10})$$

is a random vector residing in an equi-energy shell ($\mathcal{E}_m - \epsilon, \mathcal{E}_m + \epsilon$), which corresponds to a microcanonical ensemble.

A representation of the Green's function is thus achieved by employing the filtered typical pure states $\{|\psi_{\beta, \delta}^m\rangle\}$ as

$$\tilde{\mathcal{G}}_{\beta, \delta}^{AB}(\zeta) = \sum_{m=0}^{L-1} \langle \psi_{\beta, \delta}^m | A^\dagger \frac{1}{\zeta + \mathcal{E}_m - \mathcal{H}} B | \psi_{\beta, \delta}^m \rangle. \quad (\text{D11})$$

After taking appropriate limits and average over the distribution of the initial random vectors of the typical pure states, we indeed replace the canonical ensemble prescription by the typical pure state formula. By setting $\zeta = \omega + i\eta$ and

$$A = B = \hat{S}_{+\mathcal{Q}}^\alpha \equiv N^{-1/2} \sum_\ell e^{+i\mathcal{Q} \cdot r_\ell} S_\ell^\alpha, \quad (\text{D12})$$

in Eq. (D11) we obtain the dynamical spin structure factor at a momentum \mathcal{Q} and a frequency ω as

$$\begin{aligned} \tilde{S}_{\beta, \delta}(\mathcal{Q}, \omega) &= -\frac{1}{\pi} \text{Im} \sum_{\alpha=x, y, z} \sum_{m=0}^{L-1} \langle \psi_{\beta, \delta}^m | S_{-\mathcal{Q}}^\alpha \\ &\quad \times \frac{1}{\omega + i\eta + \mathcal{E}_m - \mathcal{H}} S_{+\mathcal{Q}}^\alpha | \psi_{\beta, \delta}^m \rangle, \end{aligned} \quad (\text{D13})$$

where S_ℓ^α ($\alpha = x, y, z$) is an $S=1/2$ spin operator.

In the present paper, we set E_b in Eq. (D9) as $E_b = -8.6$ ($< E_0 \simeq -8.57$) for the 24-site cluster of the Γ model. The distance among the energy grid points 2ϵ is set as

$(E_{\text{cut}} - E_b)/L$, where $L = 128$ and E_{cut} is chosen depending on T as $E_{\text{cut}} = \max\{\min\{E_b, T \ln 10^{14} + E_b\}, 4\}$. A random vector is chosen as a typical pure state $|\psi_0\rangle$ at infinite temperature. Then, a typical pure state at finite inverse temperature β is given by $|\psi_\beta\rangle = e^{-\beta\mathcal{H}/2}|\psi_0\rangle/\langle\psi_0|e^{-\beta\mathcal{H}}|\psi_0\rangle$.

APPENDIX E: HIGH-TEMPERATURE EXPANSION

Here, a high-temperature expansion (small β expansion) of static spin correlations is obtained up to third order of β . Within the language of thermal pure quantum states [31] one can write the finite-temperature expectation value of an operator O as

$$\langle O \rangle = \frac{\mathbb{E}\left[\left(\sum_v c_v^* \langle v| \right) e^{-\beta\mathcal{H}/2} O e^{-\beta\mathcal{H}/2} \left(\sum_\mu c_\mu |\mu\rangle\right)\right]}{\mathbb{E}\left[\left(\sum_v c_v^* \langle v| \right) e^{-\beta\mathcal{H}} \left(\sum_\mu c_\mu |\mu\rangle\right)\right]}, \quad (\text{E1})$$

where $\{c_v\}$ is a set of random complex numbers that satisfy the normalization $\sum_v |c_v|^2 = 1$ and the average $\mathbb{E}[\dots]$ is taken over the probability distribution of the random complex numbers. The denominator is estimated as

$$\begin{aligned} & \mathbb{E}\left[\left(\sum_v c_v^* \langle v| \right) e^{-\beta\mathcal{H}} \left(\sum_\mu c_\mu |\mu\rangle\right)\right] \\ &= 1 + \frac{\beta^2}{2N_F} \text{tr}[\mathcal{H}^2] + \frac{\beta^4}{24N_F} \text{tr}[\mathcal{H}^4] + \mathcal{O}(\beta^6), \quad (\text{E2}) \end{aligned}$$

where N_F is the Fock space dimension and $\mathbb{E}[c_v^* c_\mu] = \delta_{v,\mu}/N_F$ is used. Then, the numerator is estimated by expanding it with respect to β . The first term is

$$\begin{aligned} & \mathbb{E}\left[\left(\sum_v c_v^* \langle v| \right) O \left(\sum_\mu c_\mu |\mu\rangle\right)\right] \\ &= \sum_{v,\mu} \mathbb{E}[c_v^* c_\mu] \langle v| O |\mu\rangle \\ &= \frac{1}{N_F} \sum_v \langle v| O |v\rangle = \frac{1}{N_F} \text{tr}[O]. \quad (\text{E3}) \end{aligned}$$

The higher-order terms are given by

$$(\text{2nd term}) = -\frac{\beta}{2N_F} \text{tr}[O\mathcal{H} + \mathcal{H}O], \quad (\text{E4})$$

$$(\text{3rd term}) = \frac{\beta^2}{4N_F} \text{tr}\left[\frac{1}{2}O\mathcal{H}^2 + \mathcal{H}O\mathcal{H} + \frac{1}{2}\mathcal{H}^2O\right], \quad (\text{E5})$$

$$\begin{aligned} (\text{4th term}) &= -\frac{\beta^3}{8N_F} \text{tr}\left[\frac{1}{6}O\mathcal{H}^3 + \frac{1}{2}\mathcal{H}O\mathcal{H}^2\right. \\ &\quad \left.+ \frac{1}{2}\mathcal{H}^2O\mathcal{H} + \frac{1}{6}\mathcal{H}^3O\right]. \quad (\text{E6}) \end{aligned}$$

When O is a spin-spin correlation defined by $\prod_\ell (S_\ell^x)^{n_{\ell x}} (S_\ell^z)^{n_{\ell z}} (S_\ell^y)^{n_{\ell y}}$ ($n_{\ell\alpha} = 0, 1$), $\text{tr}[O] = 0$ or, at least, $\text{tr}[O] \ll N_F$ for $\sum_{\ell,\alpha} n_{\ell\alpha} \neq 0$, because $\text{tr}[O]/N_F$ is the expectation value $\langle O \rangle$ at $\beta = 0$. Only if O is the identity matrix, $\text{tr}[O] = N_F$.

1. yx correlation for nearest-neighbor z bond

The high-temperature expansion of $\langle S_0^y S_r^x \rangle$ for the nearest-neighbor z bonds is given as follows. The lowest order of a

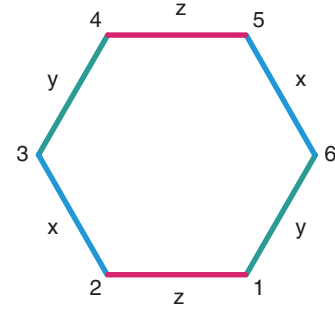


FIG. 19. Site indices used in calculations of spin correlations.

finite $\text{tr}[\mathcal{H}^m S_2^y S_1^x \mathcal{H}^n]/N_F$ (see Fig. 19 for the site indices) is given by

$$\Gamma S_2^y S_1^x \times S_2^y S_1^x = \frac{\Gamma}{16}. \quad (\text{E7})$$

When we set $O = S_2^y S_1^x$ in Eq. (E4),

$$(\text{2nd term}) = -\frac{\beta\Gamma}{16}. \quad (\text{E8})$$

2. zz correlation for nearest-neighbor z bond

The high-temperature expansion of $\langle S_0^z S_r^z \rangle$ for the nearest-neighbor z bonds is given as follows. The lowest order of a finite $\text{tr}[\mathcal{H}^m S_2^z S_1^z \mathcal{H}^n]/N_F$ (see Fig. 19 for the site indices) is, for example, given by

$$\Gamma^2 S_2^z S_1^z S_2^z S_1^z = \frac{\Gamma^2}{64}. \quad (\text{E9})$$

Then, if we set $O = S_2^z S_1^z$ in Eqs. (E4) and (E5),

$$(\text{2nd term}) = 0, \quad (\text{E10})$$

$$(\text{3rd term}) = \frac{\beta^2\Gamma^2}{64}. \quad (\text{E11})$$

3. zz correlation for third nearest neighbor

The high-temperature expansion of $\langle S_0^z S_r^z \rangle$ for the third-nearest-neighbor pairs across hexagons is given as follows. The lowest order of a finite $\text{tr}[\mathcal{H}^m S_3^z S_6^z \mathcal{H}^n]/N_F$ (see Fig. 19 for the site indices) is, for example, given by

$$\Gamma^3 S_3^z S_6^z \times S_3^z S_2^y \times S_2^y S_1^x \times S_1^z S_6^z = \frac{\Gamma^3}{256}, \quad (\text{E12})$$

or

$$\Gamma^3 S_3^z S_6^z \times S_3^z S_4^x \times S_4^x S_5^y \times S_5^y S_6^z = \frac{\Gamma^3}{256}. \quad (\text{E13})$$

Then, if we set $O = S_3^z S_6^z$ in Eqs. (E4)–(E6),

$$(\text{2nd term}) = 0, \quad (\text{E14})$$

$$(\text{3rd term}) = 0, \quad (\text{E15})$$

$$(\text{4th term}) = \frac{3\Gamma^3\beta^3}{384}. \quad (\text{E16})$$

- [1] A. Kitaev, Anyons in an exactly solved model and beyond, *Ann. Phys.* **321**, 2 (2006).
- [2] A. M. Samarakoon, A. Banerjee, S.-S. Zhang, Y. Kamiya, S. E. Nagler, D. A. Tennant, S.-H. Lee, and C. D. Batista, Comprehensive study of the dynamics of a classical Kitaev spin liquid, *Phys. Rev. B* **96**, 134408 (2017).
- [3] J. Knolle, D. L. Kovrizhin, J. T. Chalker, and R. Moessner, Dynamics of a Two-Dimensional Quantum Spin Liquid: Signatures of Emergent Majorana Fermions and Fluxes, *Phys. Rev. Lett.* **112**, 207203 (2014).
- [4] J. Knolle, D. L. Kovrizhin, J. T. Chalker, and R. Moessner, Dynamics of fractionalization in quantum spin liquids, *Phys. Rev. B* **92**, 115127 (2015).
- [5] G. Baskaran, S. Mandal, and R. Shankar, Exact Results for Spin Dynamics and Fractionalization in the Kitaev Model, *Phys. Rev. Lett.* **98**, 247201 (2007).
- [6] J. Nasu, M. Udagawa, and Y. Motome, Thermal fractionalization of quantum spins in a Kitaev model: Temperature-linear specific heat and coherent transport of Majorana fermions, *Phys. Rev. B* **92**, 115122 (2015).
- [7] J. G. Rau, E. K.-H. Lee, and H.-Y. Kee, Generic Spin Model for the Honeycomb Iridates beyond the Kitaev Limit, *Phys. Rev. Lett.* **112**, 077204 (2014).
- [8] I. Rousochatzakis and N. B. Perkins, Classical Spin Liquid Instability Driven By Off-Diagonal Exchange in Strong Spin-Orbit Magnets, *Phys. Rev. Lett.* **118**, 147204 (2017).
- [9] G. Jackeli and G. Khaliullin, Mott Insulators in the Strong Spin-Orbit Coupling Limit: From Heisenberg to a Quantum Compass and Kitaev Models, *Phys. Rev. Lett.* **102**, 017205 (2009).
- [10] W. Witczak-Krempa, G. Chen, Y. B. Kim, and L. Balents, Correlated Quantum Phenomena in the Strong Spin-Orbit Regime, *Annu. Rev. Condens. Matter Phys.* **5**, 57 (2014).
- [11] K. W. Plumb, J. P. Clancy, L. J. Sandilands, V. V. Shankar, Y. F. Hu, K. S. Burch, H.-Y. Kee, and Y.-J. Kim, α -RuCl₃: A spin-orbit assisted Mott insulator on a honeycomb lattice, *Phys. Rev. B* **90**, 041112 (2014).
- [12] J. A. Sears, M. Songvilay, K. W. Plumb, J. P. Clancy, Y. Qiu, Y. Zhao, D. Parshall, and Y.-J. Kim, Magnetic order in α -RuCl₃: A honeycomb-lattice quantum magnet with strong spin-orbit coupling, *Phys. Rev. B* **91**, 144420 (2015).
- [13] R. D. Johnson, S. C. Williams, A. A. Haghghirad, J. Singleton, V. Zapf, P. Manuel, I. I. Mazin, Y. Li, H. O. Jeschke, R. Valentí, and R. Coldea, Monoclinic crystal structure of α -RuCl₃ and the zigzag antiferromagnetic ground state, *Phys. Rev. B* **92**, 235119 (2015).
- [14] J. G. Rau, E. K.-H. Lee, and H.-Y. Kee, Spin-orbit physics giving rise to novel phases in correlated systems: Iridates and related materials, *Annu. Rev. Condens. Matter Phys.* **7**, 195 (2016).
- [15] S. M. Winter, Y. Li, H. O. Jeschke, and R. Valentí, Challenges in design of Kitaev materials: Magnetic interactions from competing energy scales, *Phys. Rev. B* **93**, 214431 (2016).
- [16] S. M. Winter, A. A. Tsirlin, M. Daghofer, J. van den Brink, Y. Singh, P. Gegenwart, and R. Valentí, Models and Materials for Generalized Kitaev Magnetism, *J. Phys.: Condens. Matter* **29**, 493002 (2017).
- [17] S. Trebst, Kitaev Materials, [arXiv:1701.07056](https://arxiv.org/abs/1701.07056).
- [18] J. A. Sears, Y. Zhao, Z. Xu, J. W. Lynn, and Y.-J. Kim, Phase diagram of α -RuCl₃ in an in-plane magnetic field, *Phys. Rev. B* **95**, 180411 (2017).
- [19] S.-H. Do, S.-Y. Park, J. Yoshitake, J. Nasu, Y. Motome, Y. S. Kwon, D. T. Adroja, D. J. Voneshen, K. Kim, T.-H. Jang, J.-H. Park, K.-Y. Choi, and S. Ji, Incarnation of Majorana fermions in Kitaev quantum spin lattice, [arXiv:1703.01081](https://arxiv.org/abs/1703.01081).
- [20] R. Henrich, A. U. B. Wolter, X. Zotos, W. Brenig, D. Nowak, A. Isaeva, T. Doert, A. Banerjee, P. Lampen-Kelley, D. G. Mandrus, S. E. Nagler, J. Sears, Y.-J. Kim, B. Büchner, and C. Hess, Unusual Phonon Heat Transport in α -RuCl₃: Strong Spin-Phonon Scattering and Field-Induced Spin Gap, *Phys. Rev. Lett.* **120**, 117204 (2018).
- [21] A. U. B. Wolter, L. T. Corredor, L. Janssen, K. Nenkov, S. Schönecker, S.-H. Do, K.-Y. Choi, R. Albrecht, J. Hunger, T. Doert, M. Vojta, and B. Büchner, Field-induced quantum criticality in the Kitaev system α -RuCl₃, *Phys. Rev. B* **96**, 041405 (2017).
- [22] S. M. Winter, K. Riedl, P. I. A. Maksimov, A. L. Chernyshev, A. Honecker, and R. Valentí, Breakdown of magnons in a strongly spin-orbital coupled magnet, *Nat. Commun.* **8**, 1152 (2017).
- [23] S. M. Winter, K. Riedl, D. Kaib, R. Coldea, and R. Valentí, Probing α -RuCl₃ Beyond Magnetic Order: Effects of Temperature and Magnetic Field, *Phys. Rev. Lett.* **120**, 077203 (2018).
- [24] A. Catuneanu, Y. Yamaji, G. Wachtel, Y. B. Kim, and H.-Y. Kee, Path to stable quantum spin liquids in spin-orbit coupled correlated materials, *npj Quantum Materials* **3**, 23 (2018).
- [25] M. Gohlke, G. Wachtel, Y. Yamaji, F. Pollmann, and Y. B. Kim, Quantum spin liquid signatures in Kitaev-like frustrated magnets, *Phys. Rev. B* **97**, 075126 (2018).
- [26] P. H. Conlon and J. T. Chalker, Spin Dynamics in Pyrochlore Heisenberg Antiferromagnets, *Phys. Rev. Lett.* **102**, 237206 (2009).
- [27] P. C. Martin, E. D. Siggia, and H. A. Rose, Statistical Dynamics of Classical Systems, *Phys. Rev. A* **8**, 423 (1973).
- [28] C. De Dominicis and L. Peliti, Field-theory renormalization and critical dynamics above T_c : Helium, antiferromagnets, and liquid-gas systems, *Phys. Rev. B* **18**, 353 (1978).
- [29] G. Wachtel and D. Orgad, Transverse thermoelectric transport in a model of many competing order parameters, *Phys. Rev. B* **90**, 224506 (2014).
- [30] A. Hams and H. De Raedt, Fast algorithm for finding the eigenvalue distribution of very large matrices, *Phys. Rev. E* **62**, 4365 (2000).
- [31] S. Sugiura and A. Shimizu, Canonical Thermal Pure Quantum State, *Phys. Rev. Lett.* **111**, 010401 (2013).
- [32] Y. Yamaji, T. Suzuki, and M. Kawamura, Numerical algorithm for exact finite temperature spectra and its application to frustrated quantum spin systems, [arXiv:1802.02854](https://arxiv.org/abs/1802.02854).
- [33] Y. Yamaji, T. Suzuki, T. Yamada, S.-i. Suga, N. Kawashima, and M. Imada, Clues and criteria for designing a Kitaev spin liquid revealed by thermal and spin excitations of the honeycomb iridate Na₂IrO₃, *Phys. Rev. B* **93**, 174425 (2016).
- [34] A. Banerjee, C. A. Bridges, J.-Q. Yan, A. A. Aczel, L. Li, M. B. Stone, G. E. Granroth, M. D. Lumsden, Y. Yiu, J. Knolle, S. Bhattacharjee, D. L. Kovrizhin, R. Moessner, D. A. Tennant, D. G. Mandrus, and S. E. Nagler, Proximate Kitaev quantum spin liquid behavior in a honeycomb magnet, *Nat. Mater.* **15**, 733 (2016).
- [35] A. Banerjee, J. Yan, J. Knolle, C. A. Bridges, M. B. Stone, M. D. Lumsden, D. G. Mandrus, D. A. Tennant, R. Moessner, and S. E. Nagler, Neutron scattering in the proximate quantum spin liquid α -RuCl₃, *Science* **356**, 1055 (2017).

- [36] An ED program package $\mathcal{H}\Phi$ is available through <https://github.com/QLMS/HPhi>
- [37] M. Kawamura, K. Yoshimi, T. Misawa, Y. Yamaji, S. Todo, and N. Kawashima, Quantum lattice model solver $\mathcal{H}\Phi$, *Comput. Phys. Commun.* **217**, 180 (2017).
- [38] M. Imada and M. Takahashi, Quantum transfer Monte Carlo method for finite temperature properties and quantum molecular dynamics method for dynamical correlation functions, *J. Phys. Soc. Jpn.* **55**, 3354 (1986).
- [39] *Maximum Entropy and Bayesian Methods*, Cambridge, England, 1988, edited by J. Skilling, Fundamental Theories of Physics (Springer Science & Business Media, New York, 1989), p. 455.
- [40] P. de Vries and H. De Raedt, Solution of the time-dependent Schrödinger equation for two-dimensional spin-1/2 Heisenberg systems, *Phys. Rev. B* **47**, 7929 (1993).
- [41] J. Jaklič and P. Prelovšek, Lanczos method for the calculation of finite-temperature quantities in correlated systems, *Phys. Rev. B* **49**, 5065 (1994).
- [42] S. Sugiura and A. Shimizu, Thermal Pure Quantum States at Finite Temperature, *Phys. Rev. Lett.* **108**, 240401 (2012).
- [43] T. Kato, On the convergence of the perturbation method, Part I, *Prog. Theor. Phys.* **4**, 514 (1949).
- [44] T. Sakurai and H. Sugiura, A projection method for generalized eigenvalue problems using numerical integration, *J. Comput. Appl. Math.* **159**, 119 (2003), *6th Japan-China Joint Seminar on Numerical Mathematics, In Search for the Frontier of Computational and Applied Mathematics toward the 21st Century*.
- [45] T. Ikegami, T. Sakurai, and U. Nagashima, A filter diagonalization for generalized eigenvalue problems based on the Sakurai–Sugiura projection method, *J. Comput. Appl. Math.* **233**, 1927 (2010).
- [46] N. Shimizu, Y. Utsuno, Y. Futamura, T. Sakurai, T. Mizusaki, and T. Otsuka, Stochastic estimation of nuclear level density in the nuclear shell model: An application to parity-dependent level density in ^{58}Ni , *Phys. Lett. B* **753**, 13 (2016).
- [47] A. Frommer, BiCGstab (ℓ) for families of shifted linear systems, *Computing* **70**, 87 (2003).